Enhanced sieving from exfoliated MoS2 membranes via covalent functionalization

Lucie Ries, Eddy Petit, Thierry Michel, Cristina Coelho Diogo, Christel Gervais, Chrystelle Salameh, Mikhael Bechelany, Sébastien Balme, Philippe Miele, Nicolas Onofrio, et al.

Enhanced sieving from exfoliated MoS_2 membranes via covalent functionalization

Lucie Ries,[1] Eddy Petit,[1] Thierry Michel,[2] Cristina Coelho Diogo,[3] Christel Gervais,[4,5] Chrystelle Salameh,[1] Mikhael Bechelany,[1] Sébastien Balme,[1] Philippe Miele,[1,5] Nicolas Onofrio,[6,*] Damien Voiry[1,*]

[1] *Institut Européen des Membranes, IEM, UMR 5635, Université Montpellier, ENSCM, CNRS, 34095 Montpellier Cedex5, France.*

[2] *Laboratoire Charles Coulomb, L2C, Université de Montpellier, CNRS, 34095 Montpellier, France.*

[3] *Sorbonne Université, Institut des Matériaux de Paris Centre (IMPC), 4 place Jussieu, 75252 Paris cedex 05, France.*

[4] *Sorbonne Université, Collège de France, Laboratoire de Chimie de la Matière Condensée de Paris (LCMCP), 4 place Jussieu, 75252 Paris cedex 05, France.*

[5] *Institut Universitaire de France (IUF), MESRI, 1 rue Descartes, 75231 Paris cedex 05, France.*

[6] *Department of Applied Physics, The Hong Kong Polytechnic University, Hong Kong, China.*

*Correspondence to: damien.voiry@umontpellier.fr; nicolas.onofrio@polyu.edu.hk.

Nanolaminate membranes made of two-dimensional materials (2D) such as graphene oxide (GO) are promising candidates for molecular sieving via size-limited diffusion in the 2D capillaries, but high hydrophilicity makes these membranes unstable in water. Here, we report a nanolaminate membrane based on covalently functionalized molybdenum disulfide (MoS_2) nanosheets. The functionalized MoS_2 membranes demonstrate >90% and ~ 87% rejection for micropollutants and NaCl respectively when operating under reverse osmotic conditions. The sieving performance and water flux of the functionalized MoS_2 membranes are attributed to both control of the capillary widths of the nanolaminates and control of the surface chemistry of the nanosheets. We identified small hydrophobic

functions, such as methyl, as the most promising functional group for water purification. Methyl functionalized nanosheets show higher water permeation rates as confirmed by our molecular dynamic simulations, while maintaining high NaCl rejection. Control of the surface chemistry and the interlayer spacing therefore offers opportunities to tune the selectivity of the membranes while enhancing their stability.

Membranes are semi-permeable barriers that allow separating contaminants depending on various parameters including their size, charge and chemical affinity. Exfoliated two-dimensional materials have demonstrated promising performance as membranes for nanofiltration and desalination [1–7]. Seminal contributions from Nair's group have shown that stacking 2D materials such as graphene oxide can be used as nanolaminate membranes [3,10]. The pore size – dictated by the capillary width between the nanosheets – enables to efficiently sieve chemical species such as small ions and molecules depending on their size [3,5]. The remarkable property of the GO membranes is attributed to the unique surface chemistry of the nanosheets combining graphene-like and oxidized domains rich in oxygenated functional groups [6,10–12]. The graphene domains of graphene oxide nanosheets enable fast water diffusion thanks to large slip length whereas the oxygenated functions play the role of spacers allowing water to penetrate in the 2D capillaries [12,13]. Unfortunately the oxygenated functional groups render GO nanosheets highly hydrophilic which causes uncontrollable swelling of the membranes [1]. The swelling of GO membranes currently limits the control of its porosity – dramatically limiting the sieving performance – and eventually leads to irreversible degradation of the membrane integrity. Other 2D materials such as transition metal dichalcogenides have been investigated as nanolaminate membranes [12,13,6,14,15]. In particular MoS_2 nanosheets have been explored as building blocks of

membranes for water purification and gas sieving [14,16]. However the use of MoS_2 remains strongly hampered by the difficulty in controlling the width of the capillaries that is found to be critical for the sieving performance [14].

Preparation and characterization of the functionalized MoS_2 membranes

We fabricated nanolaminate membranes consisting in exfoliated single-layer nanosheets of MoS_2 functionalized with different types of functional groups varying their hydrophilic character. Single layer nanosheets of MoS_2 were obtained following our previously reported method based on lithium intercalation [17,18]. Covalent functionalization of the MoS_2 nanosheets was carried out by reacting the exfoliated nanosheets with organohalide molecules[19]. We selected 3 types of organohalide molecules: iodomethane, 2-iodoethanol and 2-iodoacetamide in order to vary the polarity of the grafted functional groups. The obtained functionalized MoS_2 membranes will be now referred as acetamide-, methyl-, and ethyl-2-ol- functionalized MoS_2 membranes (Supplementary Fig. 4)[20]. The single-layer MoS_2 nanosheets were vertically stacked using vacuum filtration[3,8,21,22]. A typical functionalized MoS_2 membrane is shown in Figure 1a,b. The high stability of the MoS_2 nanosheets in solution translates into highly uniform membranes – no pinholes can be found under scanning electron microscope (SEM) (Figure 1c). The cross-section view of the membrane using SEM suggests a high degree of alignment of the nanosheets in the vertical direction (Figure 1d, Supplementary Fig. 5). High-resolution TEM images show the crystalline nature of the functionalized nanosheets (Figure 1e), while elemental mapping confirms the presence of functional groups on the surface of the nanosheets (Figure 1f). The covalent nature of the attachment of the functional groups was demonstrated by infra-red spectroscopy (Supplementary Figs. 7,8). ^{13}C CP MAS NMR was used to qualitatively assess the

covalent attachment of the functional groups by comparing the chemical shift of the aliphatic carbon (α-C) of the functional group before and after the reaction – the spectra from the organohalide molecules are presented in Supplementary Figure 10. The chemical shift from the α-C of the grafted molecules appears at 50.0 ppm, 34.7 ppm and 49.4 ppm for acetamide-, methyl- and ethyl-2-ol- functionalized MoS_2 respectively compared to -2.5 ppm, -23.2 ppm and 9 ppm for the corresponding α-C of the organohalide references (Fig. 2a) [19]. The extent of functions grafted on the nanosheets was estimated using X-Ray photoelectron spectroscopy (XPS) and the density of functional groups reaches ~ 40 at.% corresponding to a density of functional groups of ~ 4.6×10^{14} cm^{-2} (Supplementary Figs. 9-12 and Table 2).

We investigated the structure of the functionalized MoS_2 membranes using X-ray diffraction (XRD). In the case of MoS_2 membranes, an intense peak can be detected at ~ 13.9° and attributed to the (002) peak corresponding to interlayer spacing (d) of ~ 6.18 Å (Figure 2b,c). The (002) peak is slightly shifted compared to the position from bulk 2H-MoS_2 crystal confirming the quasi-perfect restacking of the nanosheets (Supplementary Fig. 14). After functionalization, the (002) peak at ~ 13.9° is displaced to lower angles at ~ 8.8°, ~ 7.5°, and ~ 8.2° for acetamide-, methyl- and ethyl-2-ol- functionalized MoS_2 respectively (Figure 2b). These displacements correspond to the increase of the interlayer spacing due to the presence of the grafted functions (Figure 2d). It is worth noting that the (002) peak from pristine MoS_2 completely disappears after functionalization suggesting that all the nanosheets in the membrane are functionalized. According to XRD and assuming a thickness of 6.15 Å for a single layer of MoS_2 – including the van der Waals radius of two sulfur atoms [See "X-Ray diffraction (XRD) on MoS_2 membranes" in the Supplementary materials] – the width of the capillary (δ) of the MoS_2 membranes varies from ~ 0.03 Å for non-functionalized MoS_2 up to ~ 5.4 Å for methyl-

functionalized MoS_2 (Figure 2b-e, Supplementary Table 3). One of the main limitation of graphene oxide membranes is the uncontrollable swelling when immerged in water, which deteriorates the sieving performance towards smaller chemical species and ions [1,23]. The functionalized MoS_2 membranes demonstrate limited swelling below than <15 % after 15 hours in water compared to ~ 65 % for graphene oxide (Figure 2e,f, Supplementary Figs. 16-18). This shows that covalent functionalization of the MoS_2 membranes increases the width of the capillaries while limiting the swelling. The effect of the functionalization of the MoS_2 nanosheets can directly be observed by contact angle measurements. Figure 2g shows the contact angle of a water droplet on pristine MoS_2 membranes compared to their functionalized counterparts. As expected, the contact angle increases with the hydrophobic nature of the grafted moieties and varies from ~ 58° up to 90° for pristine and methyl-functionalized MoS_2 respectively in perfect agreement with the decrease of the polarity of the functional groups.

Ionic and water transport in the nanolaminate membranes

We first evaluate the ionic transport across the functionalized MoS_2 membranes for various salts: LiCl, NaCl and KCl using two-compartment cells filled with a salt solution and deionized water [see "Ion permeance measurements" section in the Supplementary Information]. The functionalized membranes demonstrate low permeation rates for Li^+, Na^+ and K^+ (Figure 3a,b). The ion permeation rates for acetamide- functionalized membranes are found to strictly depend on the ionic strength, while the permeation rates for ethyl-2-ol- functionalized MoS_2 membranes do not significantly change with the increase of the ion concentration. At 1M of NaCl – corresponding to ionic strength of 1 M – the permeation rates for Na^+ are estimated to 4.2×10^{-5} ($\pm$ 8.1×10^{-6}) mol h^{-1} m^{-2} bar^{-1} and 7.6×10^{-6} ($\pm$ 1.6×10^{-6}) mol h^{-1} m^{-2} bar^{-1} for acetamide- and

ethyl-2-ol- functionalized MoS_2 membranes respectively. These values are two orders of magnitude lower than the expected permeation rates obtained from the classical diffusion law (Supplementary Table 4) [See "Permeation rate calculations" section in the Supplementary Materials]. They are also 3 orders of magnitude lower than that of graphene oxide membranes (5×10^{-2} mol h^{-1} m^{-2} bar^{-1}) and similar to the Na^+ permeation rates for graphene oxide/graphene membranes (5×10^{-5} mol h^{-1} m^{-2} bar^{-1})[1]. Such low permeation rates are attributed to the pore steric hindrance on hydrated ions as the hydrated ion diameters are typically larger than the capillary width of the functionalized MoS_2 membranes (Supplementary Table 6). Other factors such as the electrostatic interactions and the binding energy are also found to influence of the ionic transport (Supplementary Tables 5,6 and Supplementary Figs. 20,21)[5].

The effect of the nature of the functional groups on the water permeance of MoS_2 membranes was then investigated in forward (FO) and reverse osmotic (RO) configurations. The thickness of the MoS_2 membranes was precisely adjusted from 250 nm up to 2 μm by controlling the volume of MoS_2 solution to be filtered. When used as FO membranes [See "Forward osmosis-driven measurements" section in the Supplementary Materials], the flux of water reaches up to 0.15 (±0.04) L m^{-2} h^{-1} bar^{-1} for ethyl-2-ol- functionalized MoS_2 – 2.5 and 3-fold higher than that of coordinated GO and dye-decorated MoS_2 nanosheets respectively (Supplementary Fig. 23) [4,6]. We tested the MoS_2 nanolaminate membranes in RO configuration and the water flux was measured using pure water in a dead-end cell [see "Reverse osmosis (RO) measurements" section in the Supplementary Information]. Interestingly water does not flow across the non-functionalized MoS_2 membranes (Figure 3c). This observation agrees with the close-to-ideal stacking of the nanosheets. In the case of non-functionalized MoS_2, the pore size of the capillaries between two successive nanosheets is estimated to $\delta \sim 0.03$ Å – too small for letting

water permeate [14]. At the opposite water permeates through all the functionalized MoS_2 membranes. The highest water flux is obtained for ethyl-2-ol- functionalized membranes with a flux of ~ 45 L m^{-2} h^{-1} bar^{-1} for a thickness of 250 nm (Figure 3c). For comparison, the highest water flux reported for GO membrane typically remains below 10 L m^{-2} h^{-1} bar^{-1} for membranes with similar thickness [14]. Interestingly we found that the nature of the functional groups has profound effect on the permeation rate. The water flux decreases with the polarity of the functional groups demonstrating the importance of controlling the surface chemistry of the nanosheets for enhancing the water flux across the membrane (Figure 3d). We estimated the NaCl rejection from the different functionalized membranes with thickness ranging from 250 nm up to 1000 µm using a salt concentration of 0.58 wt.% (0.1 M). All the functionalized MoS_2 membranes are found efficient towards the separation of NaCl from water and the salt rejection is maintained as high as 70 % for ethyl-2-ol- functionalized MoS_2 membranes with a thickness of 250 nm for a water flux of 43 L m^{-2} h^{-1} bar^{-1} (Fig. 3c). Remarkably- the water permeation from methyl- functionalized MoS_2 membranes is largely preserved for thicknesses up to 4 µm and we measured a water flux of 24 (±0.6) L m^{-2} h^{-1} bar^{-1} for 2 µm-thick membranes – 14 times higher than ethyl-2-ol- functionalized MoS_2 membranes with same thickness (1.68 L m^{-2} h^{-1} bar^{-1}) (Supplementary Fig. 25). The behavior of methyl-functionalized MoS_2 membranes is in apparent contradiction with the expected exponential decrease of the flux as the thickness increases. This phenomenon is attributed to locally higher degree of functionalization of the nanosheets together with the hydrophobic nature of the methyl groups – responsible for its improved slip length [see "Influence of the membrane thickness on the functionalization degree and stacking order of the MoS_2 nanosheets" and "Velocity profiles and slip length estimation" sections in the Supplementary Information] [24–27].

Micropollutant removals and water desalination by reverse osmosis

To further validate our approach, we assess the performance of functionalized MoS_2 membranes for nanofiltration and desalination. We measured permeation rates for several micropollutants in RO dead-end configuration [See "Molecular sieving performances under reverse osmosis conditions" section in the Supplementary Information]. We selected four key micropollutants such as an organic dye: phtalocyanine, a psycho-active drug: caffeine, a common drug: acetaminophen, and a hormone: ß-estradiol – for which strategies of elimination are scarce and costly. We note that the micropollutants possess a large range of size from ~ 3.8 Å up ~ 10 Å (Supplementary Table 7). Our measurements reveal that the rejection: R ($R=1-C_{permeate}/C_{feed}$) for all micropollutants tested is higher than 90% while the water flux is maintained above 3 L m^{-2} h^{-1} bar^{-1} (Figure 3e). Notably, methyl- functionalized membranes are the most promising candidates towards water nano-decontamination; as the rejection reaches ~ 93 % and ~ 94 % for caffeine and acetaminophen respectively 100 % for the organic dye and ß-estradiol. We also tested the performance of membranes towards desalination in RO conditions in dead-end configuration under a pressure of 9 bar and a 0.58 wt% NaCl solution [See "Desalination performance under reverse osmosis conditions" section in the Supplementary Information]. The salt rejection peaks at 87% with a water flux of 1.6 L m^{-2} h^{-1} bar^{-1} for ethyl-2-ol- functionalized MoS_2 membranes (Fig. 3f, Supplementary Table 8). Higher water fluxes are obtained using acetamide-functionalized MoS_2 membranes, for which an 82 % NaCl rejection and a water flux of ~ 33.7 L m^{-2} h^{-1} bar^{-1} is achieved. The desalination performances from the functionalized MoS_2 membranes are superior to previous reports for 1D and 2D nanolaminate RO membranes. For instance, graphene oxide RO membranes exhibit a NaCl rejection of ~ 40 % with a water flux of

4 L m^{-2} h^{-1} bar^{-1} when using a salt concentration of 0.12 wt.% and under 5 bar[5]. Our results also compare favorably to the performance of nanolaminate RO membranes based on graphene oxide (GO)/graphene hybrids that demonstrate a ~ 75% NaCl rejection with a water flux of < 0.46 L m^{-2} h^{-1} bar^{-1} when using a 0.58 wt.% NaCl solution (Supplementary Table 9)[28]. The functionalized MoS_2 RO membranes also outperform hybrid GO/GO quantum dots and GO/carbon nanotubes RO membranes that exhibit NaCl rejections of 15 % and 59 % for water fluxes of 128 L m^{-2} h^{-1} bar^{-1} and 5.5 L m^{-2} h^{-1} bar^{-1} for a NaCl concentration of 0.02 and 0.06 wt.% respectively (Supplementary Table 9)[29,30].

Molecular dynamic simulations of water flux

In a view to rationalize the experimental results, we performed classical molecular dynamics simulations of water transport in the different functionalized MoS_2 nanochannels [see "Molecular dynamics simulations" section in the Supplementary Information]. To describe with precision the potential chemistry between water, functional groups and MoS_2, including partial charge transfer and polarization effects, we performed reactive simulations[29]. Simulation cells consist in two water reservoirs separated by a nanochannel, and the external pressure is controlled using the fluctuating wall method[30]. A snapshot of a typical simulation cell is presented in Figure 4a. We first study the water flux inside pristine MoS_2 as a function of channel width. Within the timescale of MD simulations, we did not observe any water molecule penetrating inside a MoS_2 channel of 8 Å width. When increasing the capillary width, the predicted water fluxes quickly rise to 1.1, 5.3, 110.5, 499.0, 1241.0 and 3302.0 L m^{-2} h^{-1} bar^{-1} for spacings of 10, 12, 14, 16, 18 and 20 Å, respectively (Figure 4b). The water flux was evaluated for the different types of MoS_2 membranes at a fixed interlayer spacing of 12 Å (Figure 4f). We

note that such value of interlayer spacing width is larger than that measured experimentally for non-functionalized MoS_2 membranes. Fluxes predicted by MD simulation reach 5.3, 13.0, 1.9 and 3.2 L m^{-2} h^{-1} bar^{-1} for pristine MoS_2, methyl-, acetamide- and ethyl-2-ol- functionalized MoS_2 membranes in agreement with the experimental trend presented in Figure 3c.

To understand the effect of functionalization on the water flux, we studied the organization of water molecules in the various MoS_2 nanochannels, under pressure. We computed density profiles and axial density function (ADF) of water confined in the channels. [See "Density profiles" and "Axial density function" section in the Supplementary Information]. For pristine channels, we found that water molecules are highly organized in layers (Supplementary Fig. 37) and along the flux direction with a period of ~3 Å (Fig. 4c). Interestingly water molecules typically sit on top of sulfur atoms (Figure 4c,d). Such organization of confined water is in agreement with recent simulations of water between MoS_2 [33]. ADF of water molecules between methyl-functionalized MoS_2 shows minimal structure along the flux direction while no structure is observed between acetamide and ethyl-2-ol functionalized layers (Figure 4d). We further calculated the hydrogen bond correlation function [34]. We found lifetimes of ~1 ns for water inside 12 Å MoS_2 capillaries, two orders of magnitude larger than in bulk water and characteristic of an ice-like structure. The presence of non-polar functional groups such as methyl lowers lifetimes by a factor of 2 leading to more bulk-like water (Supplementary Fig. 39).

To correlate the water dynamics to the nature of the nanochannel, we analyzed the velocity of water molecules in contact with pristine and methyl-functionalized MoS_2. Figure 4e displays the time-averaged water velocity map in the XZ plane (under constant pressure) and its projection along the channel direction (Supplementary Figs. 40,41). The positions of sulfur atoms are indicated by white and black dashed lines in the velocity map and its projection, respectively.

We predict smaller velocity of water molecules located right under S-atoms. These locations represent "pinning points", electrostatic in nature, between highly polarized O-H and Mo-S bonds. This suggests that S-atoms provide the template for the water structure. The presence of methyl groups substitutes some of these pinning points and enhances the velocity of water molecules located right below them. Our numerical simulations also reveal that methyl groups enhance the water flux by improving the water slip length and limiting the steric effect compared to other larger functional groups (Supplementary Figs. 31,42,43).

Outlook

We have shown that covalent functionalization of exfoliated nanosheets can efficiently control the interlayer spacing and enhance the sieving performance of the nanolaminate membranes. The functionalized MoS_2 membranes demonstrate remarkable performance towards water purification and desalination compared to the current state of the art. Our experimental results suggest that small, hydrophobic functional groups such as methyl, are key for enhancing the water flow in MoS_2 membranes as supported by our molecular dynamic simulations. We believe our strategy paves the way to the preparation of membranes with tunable sieving behaviour. The control of the surface chemistry of exfoliated 2D materials allows further exploring nanofluidic phenomena inside nanolaminate membranes at fundamental and practical levels for water purification or osmotic energy.

References

1. Abraham, J. *et al.* Tunable sieving of ions using graphene oxide membranes. *Nat. Nanotechnol.* **12**, 546–550 (2017).
2. Kim, H. W. *et al.* Selective Gas Transport Through Few-Layered Graphene and Graphene Oxide Membranes. *Science* **342**, 91–95 (2013).
3. Joshi, R. K. *et al.* Precise and Ultrafast Molecular Sieving Through Graphene Oxide Membranes. *Science* **343**, 752–754 (2014).
4. Chen, L. *et al.* Ion sieving in graphene oxide membranes via cationic control of interlayer spacing. *Nature* **550**, 380–383 (2017).
5. Han, Y., Xu, Z. & Gao, C. Ultrathin Graphene Nanofiltration Membrane for Water Purification. *Adv. Funct. Mater.* **23**, 3693–3700 (2013).
6. Hirunpinyopas, W. *et al.* Desalination and Nanofiltration through Functionalized Laminar MoS_2 Membranes. *ACS Nano* **11**, 11082–11090 (2017).
7. Heiranian, M., Farimani, A. B. & Aluru, N. R. Water desalination with a single-layer MoS_2 nanopore. *Nat. Commun.* **6**, 8616 (2015).
8. Nair, R. R., Wu, H. A., Jayaram, P. N., Grigorieva, I. V. & Geim, A. K. Unimpeded permeation of water through helium-leak-tight graphene-based membranes. *Science* **335**, 442–444 (2012).
9. Koltonow, A. R. & Huang, J. Two-dimensional nanofluidics. *Science* **351**, 1395–1396 (2016).
10. Wei, N., Peng, X. & Xu, Z. Understanding Water Permeation in Graphene Oxide Membranes. *ACS Appl. Mater. Interfaces* **6**, 5877–5883 (2014).

11. Wei, N., Peng, X. & Xu, Z. Breakdown of fast water transport in graphene oxides. *Phys. Rev. E* **89**, 012113 (2014).

12. Sun, L., Huang, H. & Peng, X. Laminar MoS_2 membranes for molecule separation. *Chem. Commun.* **49**, 10718–10720 (2013).

13. Sun, L. *et al.* Ultrafast Molecule Separation through Layered WS_2 Nanosheet Membranes. *ACS Nano* **8**, 6304–6311 (2014).

14. Wang, Z. *et al.* Understanding the Aqueous Stability and Filtration Capability of MoS_2 Membranes. *Nano Lett.* **17**, 7289–7298 (2017).

15. Deng, M., Kwac, K., Li, M., Jung, Y. & Park, H. G. Stability, Molecular Sieving, and Ion Diffusion Selectivity of a Lamellar Membrane from Two-Dimensional Molybdenum Disulfide. *Nano Lett.* **17**, 2342–2348 (2017).

16. Achari, A., S, S. & Eswaramoorthy, M. High performance MoS_2 membranes: effects of thermally driven phase transition on CO_2 separation efficiency. *Energy Environ. Sci.* **9**, 1224–1228 (2016).

17. Joensen, P., Frindt, R. F. & Morrison, S. R. Single-layer MoS_2. *Mater. Res. Bull.* **21**, 457–461 (1986).

18. Eda, G. *et al.* Photoluminescence from Chemically Exfoliated MoS_2. *Nano Lett.* **11**, 5111–5116 (2011).

19. Voiry, D. *et al.* Covalent functionalization of monolayered transition metal dichalcogenides by phase engineering. *Nat. Chem.* **7**, 45–49 (2015).

20. Wang, H. *et al.* $MoSe_2$ and WSe_2 Nanofilms with Vertically Aligned Molecular Layers on Curved and Rough Surfaces. *Nano Lett.* **13**, 3426–3433 (2013).

21. Eda, G., Fanchini, G. & Chhowalla, M. Large-area ultrathin films of reduced graphene oxide as a transparent and flexible electronic material. *Nat. Nanotechnol.* **3**, 270–274 (2008).

22. Acerce, M., Voiry, D. & Chhowalla, M. Metallic 1T phase MoS_2 nanosheets as supercapacitor electrode materials. *Nat. Nanotechnol.* **10**, 313–318 (2015).

23. Yeh, C.-N., Raidongia, K., Shao, J., Yang, Q.-H. & Huang, J. On the origin of the stability of graphene oxide membranes in water. *Nat Chem* **7**, 166–170 (2015).

24. Holt, J. K. *et al.* Fast Mass Transport Through Sub-2-Nanometer Carbon Nanotubes. *Science* **312**, 1034–1037 (2006).

25. Secchi, E. *et al.* Massive radius-dependent flow slippage in carbon nanotubes. *Nature* **537**, 210–213 (2016).

26. Balme, S. *et al.* Unexpected ionic transport behavior on hydrophobic and uncharged conical nanopore. *Faraday Discuss.* **210**, 69-85 (2018).

27. Balme, S. *et al.* Ionic transport through sub-10 nm diameter hydrophobic high-aspect ratio nanopores: experiment, theory and simulation. *Sci. Rep.* **5**, 10135 (2015).

28. Morelos-Gomez, A. *et al.* Effective NaCl and dye rejection of hybrid graphene oxide/graphene layered membranes. *Nat. Nanotechnol.* **12**, 1083–1088 (2017).

29. Han, Y., Jiang, Y. & Gao, C. High-Flux Graphene Oxide Nanofiltration Membrane Intercalated by Carbon Nanotubes. *ACS Appl. Mater. Interfaces* **7**, 8147–8155 (2015).

30. Zhao, G., Hu, R., Zhao, X., He, Y. & Zhu, H. High flux nanofiltration membranes prepared with a graphene oxide homo-structure. *J. Membr. Sci.* **585**, 29–37 (2019).

31. van Duin, A. C. T., Dasgupta, S., Lorant, F. & Goddard, W. A. ReaxFF: A Reactive Force Field for Hydrocarbons. *J. Phys. Chem. A* **105**, 9396–9409 (2001).

32. Lupkowski, M. & van Swol, F. Computer simulation of fluids interacting with fluctuating walls. *J. Chem. Phys.* **93**, 737–745 (1990).

33. Kwac, K. *et al.* Multilayer Two-Dimensional Water Structure Confined in MoS_2. *J. Phys. Chem. C* **121**, 16021–16028 (2017).

34. Chandra, A. Effects of ion atmosphere on hydrogen-bond dynamics in aqueous electrolyte solutions. *Phys. Rev. Lett.* **85**, 768 (2000).

Acknowledgments

L.R. acknowledges scholarship from the Graduate School "Ecole doctorale des Sciences Chimiques Balard, ED 459". D.V. acknowledges financial supports from "Project Axe Transverse Santé" and CNRS Cellule Energie exploratory project: "NANOSMO". This project has also received partial funding from the European Research Council (ERC) under the European Union's Horizon 2020 research and innovation programme (grant agreement No 804320). The French Région Ile de France - SESAME program is acknowledged for financial support (700 MHz NMR spectrometer). We thank The Hong Kong Polytechnic University and the department of Applied Physics for the computational resources. Didier Cot and Erwan Oliviero are acknowledged for the electron microscopy. We thank Valérie Flaud and Léa Causse for the XPS and the ICP-OES measurements.

Author Contributions

D.V. conceived the idea, designed the experiments and wrote the manuscript. L.R. designed the experiments with D.V., fabricated the membranes and performed membrane characterizations

and analyzed the results. L.R. and D.V. analyzed the data and wrote the manuscript. E.P. carried out HPLC and liquid NMR spectroscopy measurements. T.M. performed RAMAN measurements with L.R. and discussed the results with D.V. and L.R.. C.C.D. and C.G. performed ^{13}C CAS NMR spectroscopy measurements and C.S. discussed the results with D.V. and L.R.. S.B. and M.B. assisted L.R. on ionic permeation experiments and discussed the water permeation results. N.O. performed the Molecular dynamic simulations and wrote the manuscript with D.V. and L.R.. P.M. discussed the results with D.V. and L.R. All of the authors edited the manuscript before submission.

Competing financial interests

The authors declare no competing financial interests.

Data availability

The data that support the plots within this paper and other findings of this study are available from the corresponding authors upon reasonable request.

Methods

Synthesis of exfoliated single-layer MoS_2 nanosheets

MoS_2 nanosheets were prepared via lithium intercalation method as reported previously. 0.4 g of bulk crystal of MoS_2 was mixed with 4 mL of n-butyllithium in hexane and refluxed for 48 h under argon [18]. The intercalated powder was then recovered by vacuum filtration and washed several times with hexane (4x50 mL). The intercalated powder was exfoliated in water at 1mg/mL and sonicated for 1 h to facilitate the exfoliation. The solution was then centrifuged to

remove all lithium cations as well as the non-exfoliated materials [35]. The single-layer nature of the exfoliated nanosheets has previously been characterized [18].

Functionalization of single-layer MoS_2 nanosheets

Single-layer MoS_2 nanosheets were functionalized using organohalide reagents. Functionalization of the nanosheets was performed either in solution or directly on the membranes. In liquid phase, the reagents were added to the MoS_2 solution with a 10-fold excess. After 48 h, the solution was filtered on the polymeric support in order to fabricate the functionalized membranes following the method described above. Alternatively MoS_2 nanosheets were functionalized after the fabrication of the membranes by diffusing the reactant solution through the lamellar structure. The membranes made of MoS_2-Acet. and MoS_2-EtOH were functionalized in solution prior the fabrication of the nanolaminate membranes. MoS_2-Met. membranes were functionalized directly on the porous support after the filtration of the MoS_2 nanosheets. The non-functionalized MoS_2 solution was first filtered over a nylon membrane with 220-nm pore-size. After all the solution was filtered, the solution of organohalide reagents (for example iodomethane) – in 10-fold excess – dissolved in water:2-propanol (2:1 in volume) was carefully poured in the filtration funnel while the MoS_2 membrane remains fully wet. The reagent solution was let to slowly diffuse through the MoS_2 membrane for 48 hours after what the membrane was rinsed with 2-propanol (4×50 mL), ethanol (4×50 mL) and water (4×50 mL).

Fabrication of MoS_2 membranes

The MoS_2 membranes were prepared by vacuum filtration as described previously[36]. Briefly, the solution of exfoliated single-layer MoS_2 nanosheets was filtered over porous polymeric supports with 25 nm and 220 nm pore sizes. Examples of polymeric support are typically made of

nitrocellulose, nylon, PVDF. In this study, we used Nylon supports with 200 nm pore size for testing all the MoS_2-based membranes. The size of the filtration apparatus was 3.5 cm in diameter. The as-prepared MoS_2 membranes were then cut to a size of approx. 1 cm^2 in order to confirm the reproducibility of the performance for the same batch. At least 4 membranes were tested for each batch. We also fabricated and tested MoS_2 membranes from different batches in order to confirm the reproducibility of the results.

We measured that the density of the MoS_2 membranes is ~5.2 g cm^{-3}. The porosity of the MoS_2 membranes was estimated using the equation:

$$\phi = 1 - \frac{\rho_{membranes}}{\rho_{MoS_2}} \quad (1)$$

where $\rho_{membranes}$ and ρ_{MoS_2} are the density of the membrane and bulk MoS_2 (5.09 g cm^{-3}), respectively. The density of the non-functionalized MoS_2 membranes varies of only 5% compared to the density of bulk crystal. This indicates that the turbostatic stacking of the MoS_2 nanosheets in the membrane is close to the stacking of 2H MoS_2 crystals suggesting a dense structure.

Molecular dynamics simulations

Simulations cells were built starting from a 6-atoms orthogonal primitive cell of MoS_2 in the 1T' phase [37] and replicated 20×8 in the in-plane directions to create one of the (upper and lower) channel wall. The curved region was achieved by bending to 90° 4 unit cells symmetrically along the long direction. This geometry insured a faster filling of the water molecule inside the channel. To further speed-up filling, water molecules were introduced using VMD [38] in both reservoirs and inside the nanochannel (for $\delta \geq 10$ Å). C, H, O and N force field parameters were

taken from Ref. 39 and combined with that of MoS_2 from Ref. 40. We slightly modified the S-O van der Waals parameters to improve the water/MoS_2 interactions [see "Reactive MD and interatomic potential" in the Supplementary Information]. All simulations were performed with the large-scale MD package LAMMPS [41] with a time step of 0.5 fs in the NPT ensemble at 300 K and under 1 Atmosphere in the periodic directions. Periodic boundary conditions were applied along the directions perpendicular to the channel. Simulation cells were minimized and equilibrated for a short 5 ps run without external pressure followed by 500 ps under an applied pressure of 500 MPa to reach steady-state.

References

35. Kappera, R. *et al.* Phase-engineered low-resistance contacts for ultrathin MoS_2 transistors. *Nat. Mater.* **13**, 1128–1134 (2014).
36. Acerce, M., Voiry, D. & Chhowalla, M. Metallic 1T phase MoS_2 nanosheets as supercapacitor electrode materials. *Nat. Nanotechnol.* **10**, 313–318 (2015).
37. Voiry, D. *et al.* Covalent functionalization of monolayered transition metal dichalcogenides by phase engineering. *Nat. Chem.* **7**, 45–49 (2015).
38. Humphrey, W., Dalke, A. & Schulten, K. VMD: visual molecular dynamics. *J. Mol. Graph.* **14**, 33–38 (1996).
39. Kim, S.-Y. & van Duin, A. C. T. Simulation of Titanium Metal/Titanium Dioxide Etching with Chlorine and Hydrogen Chloride Gases Using the ReaxFF Reactive Force Field. *J. Phys. Chem. A* **117**, 5655–5663 (2013).
40. Ostadhossein, A. *et al.* ReaxFF Reactive Force-Field Study of Molybdenum Disulfide (MoS_2). *J. Phys. Chem. Lett.* **8**, 631–640 (2017).
41. Plimpton, S. Fast Parallel Algorithms for Short-Range Molecular Dynamics. *J. Comput. Phys.* **117**, 1–19 (1995).

Figure 1 | Nanolaminate membranes made of covalently functionalized MoS_2 nanosheets. a-b, Photographs of a functionalized MoS_2 membrane prepared by vacuum filtration. **c**, Top view of a functionalized MoS_2 membrane observed by scanning electron microscope (SEM). **d**, Side view of a functionalized MoS_2 membrane observed by SEM showing the high degree of the alignment of the vertically stacked MoS_2 nanosheets forming 2D capillaries. **e**, High-resolution Transmission Electron Microscope (TEM) images of MoS_2 nanosheets functionalized with acetamide groups. Interlayer spacing of ~ 10.1 Å can be observed from vertically aligned nanosheets (left) whereas the basal plane of the nanosheets are found crystalline (right) as confirmed by the diffraction pattern (inset). **f**, Energy Dispersive X-ray mapping of the Mo (in red) and N (in blue) elements from acetamide- functionalized MoS_2 nanosheets.

Figure 2 | Characterization of the functionalized MoS_2 membranes. a, ^{13}C CP MAS NMR spectra for the different covalently functionalized MoS_2 nanosheets. The peaks corresponding to the α-C of the functional groups are detected at ~50 ppm, 34.7 ppm and 49.7 ppm for acetamide-, methyl- and ethyl-2-ol- functionalized MoS_2 respectively. **b**, X-ray diffraction spectra from pristine non-functionalized MoS_2 membranes (blue) and functionalized MoS_2 membranes with acetamide (MoS_2-Acet.; black), methyl (MoS_2-Met.; green) and ethyl-2-ol (MoS_2-EtOH; orange). After functionalization the (002) peaks of the MoS_2 nanosheets appear shifted towards lower angles due to the presence of the functional groups. **c-d**, Schematics of restacked MoS_2 nanosheets (**c**) and acetamide-functionalized MoS_2 (**d**) with the interlayer spacing: d and the capillary width: δ. **e**, Evolution of the capillaries width from the MoS_2 membranes when immerged in water. **f**, Swelling of the graphene oxide membranes (in red) compared to the MoS_2

membranes. **g**, Contact angle measurements from MoS_2 and functionalized MoS_2 membranes. The contact angle can to be tuned from 58° for pristine MoS_2 up to 90° for methyl-functionalized MoS_2. All error bars correspond to standard deviation of at least 4 samples.

Figure 3 | Performance of the functionalized MoS_2 membranes towards water purification and desalination. a,b Permeation rates for Na^+, Li^+ and K^+ across acetamide- functionalized (**a**) and ethyl-2-ol- functionalized (**b**) MoS_2 membranes measured for different ionic strengths under forward osmosis. Chloride was used as counter ion in all the cases. The permeation rates are relatively stable even for the highest ionic strength corresponding to 1M feed solutions. **c**, Water flux (dashed lines) and salt rejection (dotted lines) measured from MoS_2 and functionalized-MoS_2 membranes under reverse osmosis. The water fluxes have been obtained in dead end configuration using pure water. High water flux is observed for all functionalized MoS_2 membranes whereas the flux is suppressed in the absence of functional groups. **d**, Evolution of the water flux with the water contact angle of the functionalized membranes. **e**, Rejection of different micropollutants measured for the functionalized MoS_2 membranes measured under a pressure of 2 bars. **f**, Comparison of the desalination performance from 500 nm-thick functionalized MoS_2 membranes measured at 9 bar using a 0.58 wt.% NaCl solution with other membranes made of carbon nanotubes, graphene oxide and their hybrids as well as polymeric membranes based on Thin Film Composite (TFC) technology. All error bars correspond to standard deviation of at least 4 samples. We note that the salt concentration may differ between the experiments. The direct comparison of the desalination performance of the MoS_2 membranes with previous results from the literature can be found in Supplementary Table 9.

Figure 4 | Molecular dynamics simulations of water transport in 2D nanochannels. a, Snapshot of a typical atomistic model used in the simulations with the x, y and z axes. The fluctuating wall method is used to control pressure in the water reservoirs. Periodic boundary conditions are applied in the y- and z-direction. **b**, Number of water molecules crossing the mid-point of the nanochannel as a function of simulation time for various interlayer spacings (*d*). The logarithmic of the flux versus the interlayer spacing is represented in the inset. The water flux varies as the cubic power of the spacing. **c**, Snapshots zooming-in the nanochannels of various functionalized MoS_2 nanosheets. **d**, Axial density function representing the probability of finding a water molecule from a reference water molecule. For pristine case, we can clearly identify the structure of water in the axial direction with a period of approximately 3 Å while no clear structure is observed for the functionalized cases. **e**, Time averaged velocity map of the first layer of water molecules in the xz plane and its projection along the channel direction (v_x). The velocity of water molecules is enhanced by the presence of methyl groups. **f**, Number of water molecules crossing the mid-point of the nanochannel as a function of simulation time for the 4 channels described in (**c**). The corresponding water fluxes are summarized in the inset. The fluxes are normalized to surface of the nanochannel. Methyl-functionalized MoS_2 channel enhances water flux.

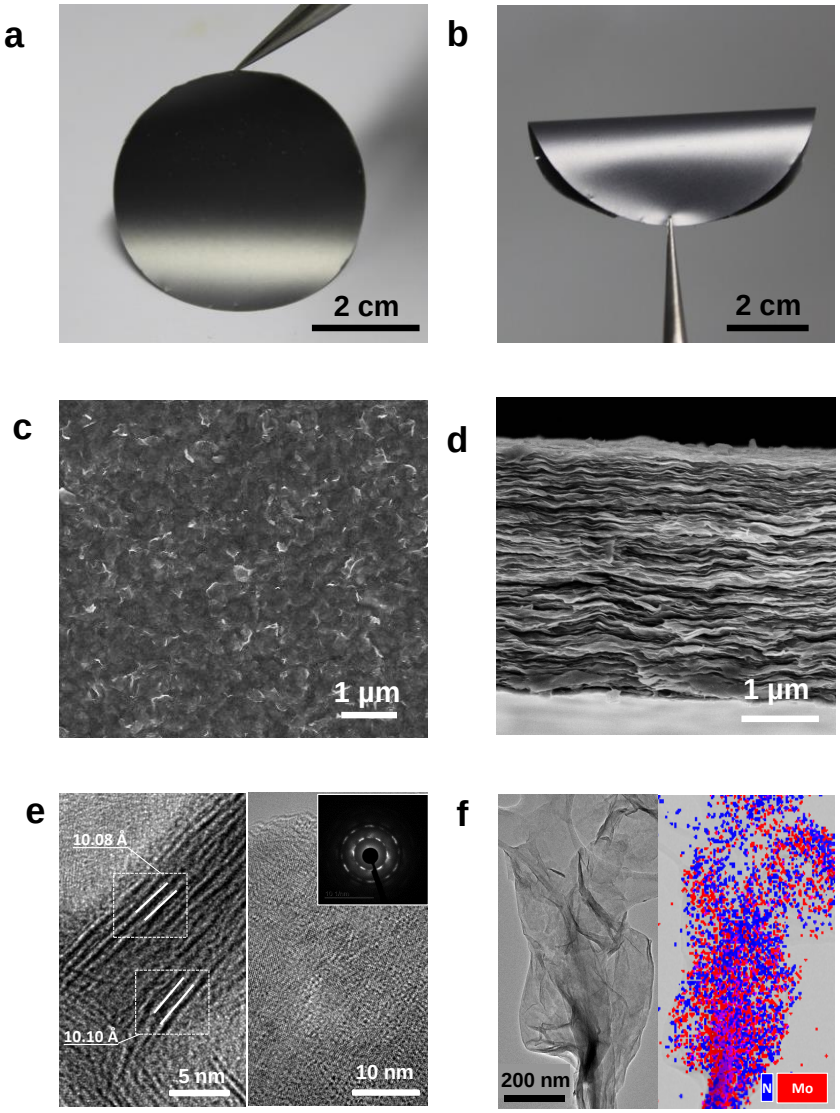
a
2 cm
b
2 cm
c
1 μm
d
1 μm
e
10.08 Å
10.10 Å
5 nm
10 nm
f
200 nm
N
Mo

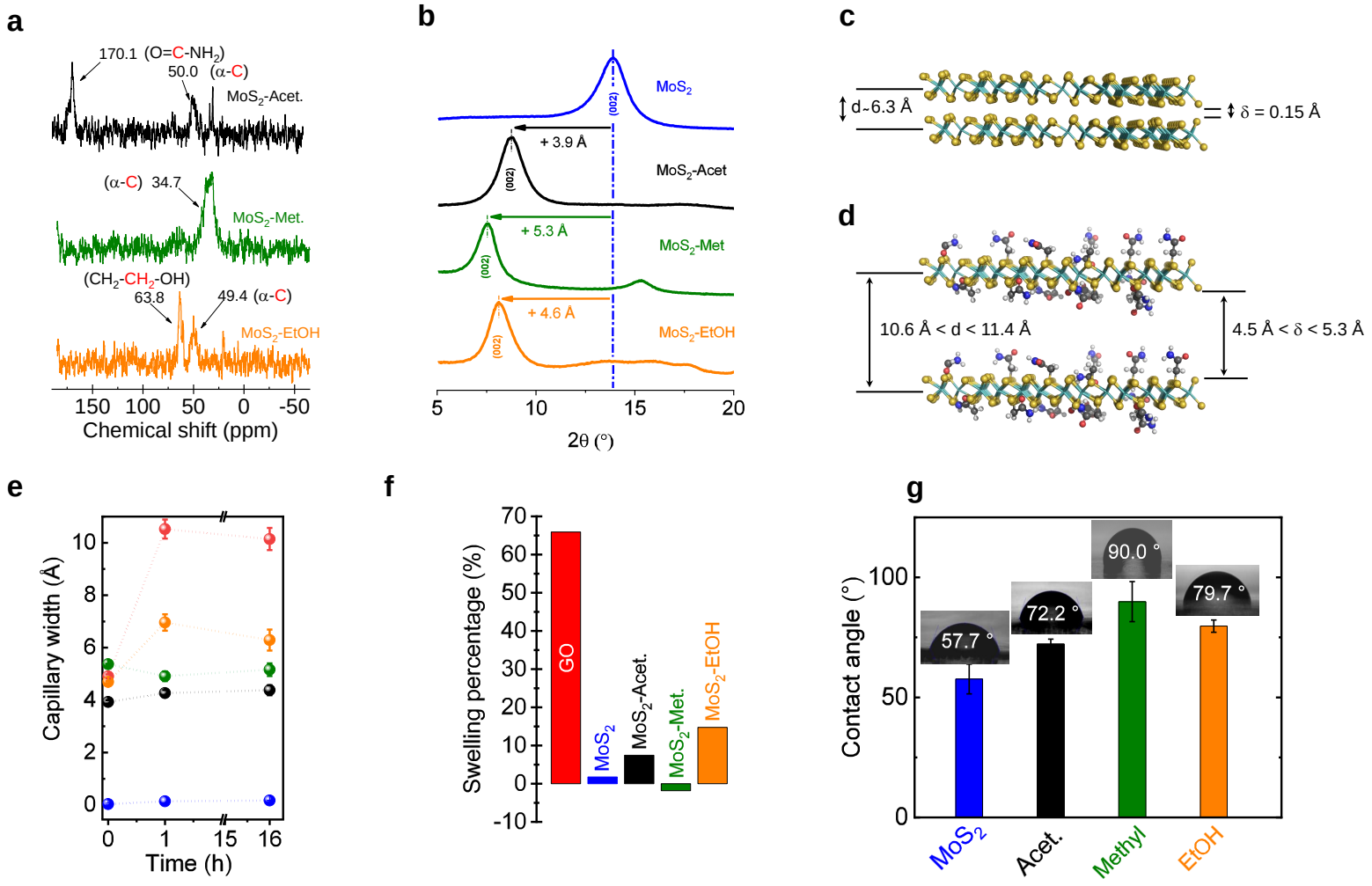
a
170.1 (O=C-NH2)
50.0 (α-C)
MoS2-Acet.
(α-C) 34.7
MoS2-Met.
(CH2-CH2-OH)
63.8
49.4 (α-C)
MoS2-EtOH
150 100 50 0 -50
Chemical shift (ppm)
b
MoS2
(002)
+ 3.9 Å
MoS2-Acet
+ 5.3 Å
MoS2-Met
+ 4.6 Å
MoS2-EtOH
5 10 15 20
2θ (°)
c
d~6.3 Å
δ = 0.15 Å
d
10.6 Å < d < 11.4 Å
4.5 Å < δ < 5.3 Å
e
Capillary width (Å)
0 2 4 6 8 10
0 1 15 16
Time (h)
f
Swelling percentage (%)
70 60 50 40 30 20 10 0 -10
GO
MoS2
MoS2-Acet.
MoS2-Met.
MoS2-EtOH
g
Contact angle (°)
100 50 0
57.7 °
72.2 °
90.0 °
79.7 °
MoS2
Acet.
Methyl
EtOH

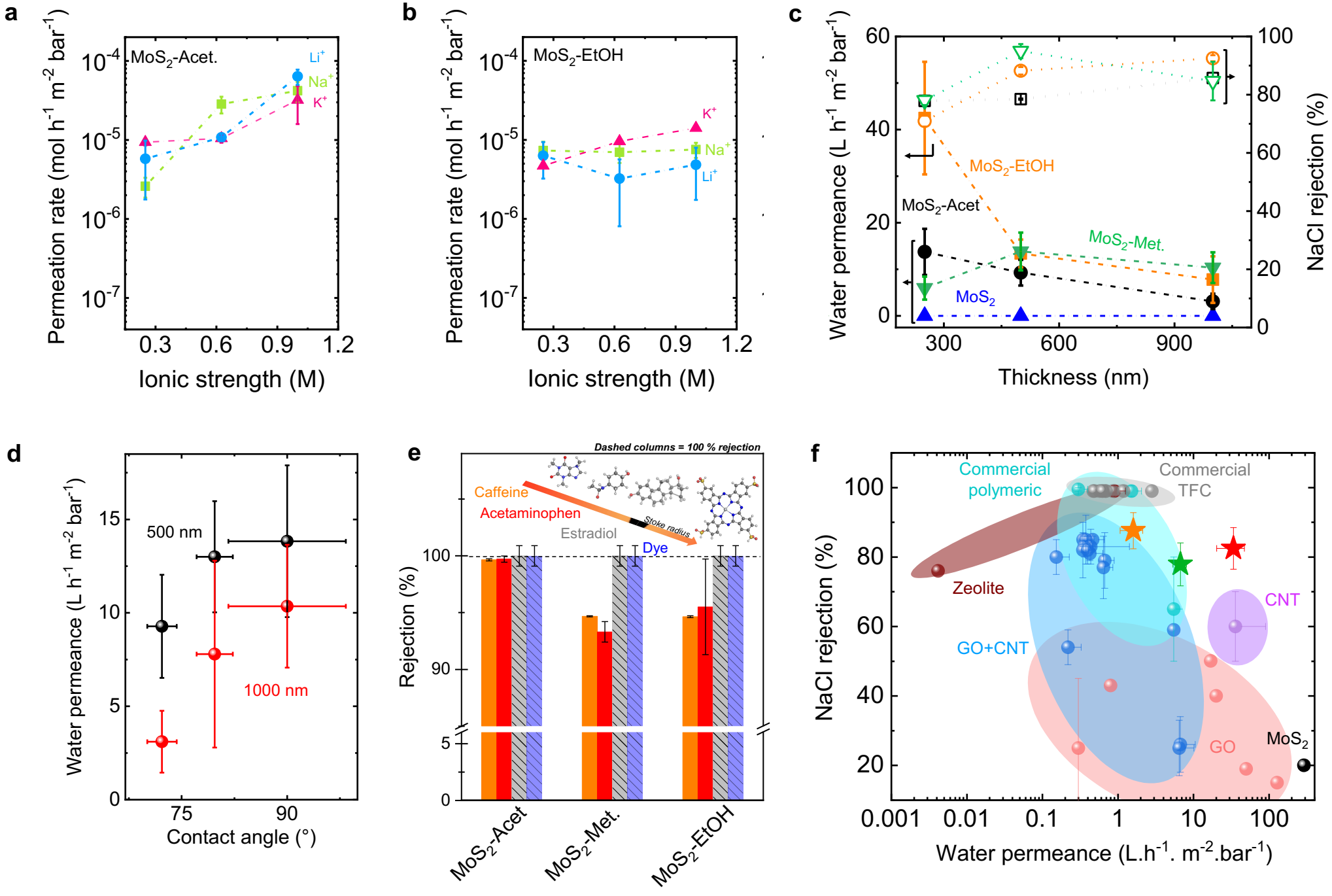
a
MoS2-Acet.
Li+
Na+
K+
Permeation rate (mol h-1 m-2 bar-1)
Ionic strength (M)
b
MoS2-EtOH
K+
Na+
Li+
Permeation rate (mol h-1 m-2 bar-1)
Ionic strength (M)
c
MoS2-EtOH
MoS2-Acet
MoS2-Met.
MoS2
Water permeance (L h-1 m-2 bar-1)
NaCl rejection (%)
Thickness (nm)
d
500 nm
1000 nm
Water permeance (L h-1 m-2 bar-1)
Contact angle (°)
e
Dashed columns = 100 % rejection
Caffeine
Acetaminophen
Estradiol
Dye
Stoke radius
Rejection (%)
MoS2-Acet
MoS2-Met.
MoS2-EtOH
f
Commercial polymeric
Commercial TFC
Zeolite
CNT
GO+CNT
GO
MoS2
NaCl rejection (%)
Water permeance (L.h-1. m-2.bar-1)

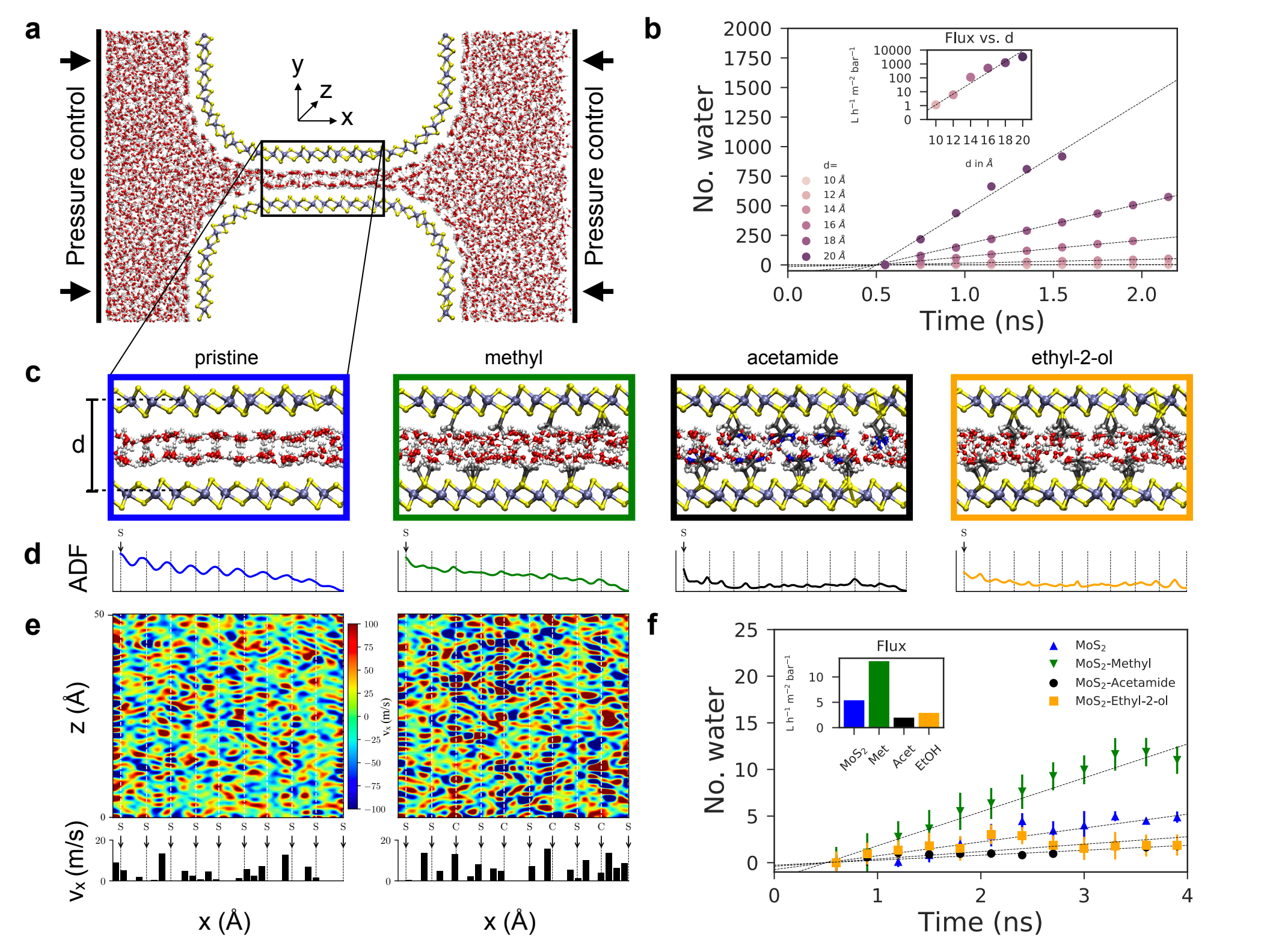
a
Pressure control
Pressure control
y
z
x
b
No. water
Time (ns)
Flux vs. d
L h⁻¹ m⁻² bar⁻¹
d in Å
d=
10 Å
12 Å
14 Å
16 Å
18 Å
20 Å
c
pristine
methyl
acetamide
ethyl-2-ol
d
d
ADF
S
e
z (Å)
vx (m/s)
x (Å)
x (Å)
f
No. water
Time (ns)
Flux
L h⁻¹ m⁻² bar⁻¹
MoS2
Met
Acet
EtOH
MoS2
MoS2-Methyl
MoS2-Acetamide
MoS2-Ethyl-2-ol

Supplementary Materials for

Enhanced sieving from exfoliated MoS_2 membranes via covalent functionalization

Lucie Ries,[1] Eddy Petit,[1] Thierry Michel,[2] Cristina Coelho Diogo,[3] Christel Gervais,[4,5] Chrystelle Salameh,[1] Mikhael Bechelany,[1] Sébastien Balme,[1] Philippe Miele,[1,5] Nicolas Onofrio,[6,*] Damien Voiry[1,*]

[1] *Institut Européen des Membranes, IEM, UMR 5635, Université Montpellier, ENSCM, CNRS, 34095 Montpellier Cedex5, France.*

[2] *Laboratoire Charles Coulomb, L2C, Université de Montpellier, CNRS, 34095 Montpellier, France.*

[3] *Sorbonne Université, Institut des Matériaux de Paris Centre (IMPC), 4 place Jussieu, 75252 Paris cedex 05, France.*

[4] *Sorbonne Université, Collège de France, Laboratoire de Chimie de la Matière Condensée de Paris (LCMCP), 4 place Jussieu, 75252 Paris cedex 05, France.*

[5] *Institut Universitaire de France (IUF), MESRI, 1 rue Descartes, 75231 Paris cedex 05, France.*

[6] *Department of Applied Physics, The Hong Kong Polytechnic University, Hong Kong, China.*

*Correspondence to: damien.voiry@umontpellier.fr; nicolas.onofrio@polyu.edu.hk.

Supplementary Materials

Table of content

Materials and Methods

Bulk MoS_2 powder, iodomethane, 2-iodoacetamide, 2-iodoethanol (> 99 %), acetamide, n-butyllithium (1.6 M in hexane) and Nickel(II) phthalocyanine-tetrasulfonic acid tetrasodium salt were purchased from Sigma Aldrich. Organic solvents were ordered from either Sigma Aldrich or Alfa Aesar and used as received.

Size distribution of the single-layer MoS_2 nanosheets

The size of the single-layer nanosheets was analyzed by atomic force microscopy (Digital Instruments Nanoscope IV in tapping mode with standard cantilevers with spring constant of 40 N/m and tip curvature <10 nm). Supplementary Figure 1 shows the statistics of the size distribution of the exfoliated MoS_2 nanosheets. The average length and width are estimated to 340 and 230 nm respectively.

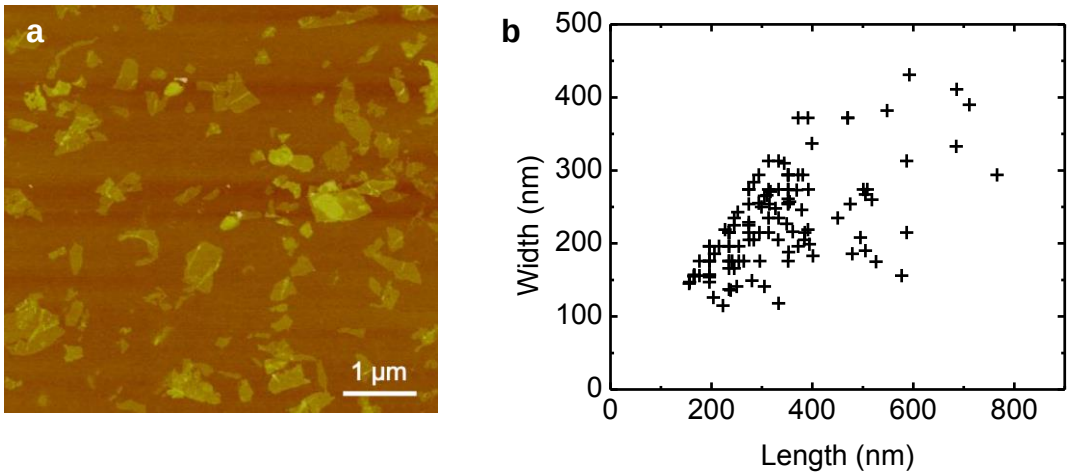

Supplementary Figure 1. (**a**) AFM image of chemically exfoliated MoS_2 nanosheets. (**b**) Size distribution of the exfoliated MoS_2 nanosheets measured by Atomic Force Microscopy.

Zeta potential measurements

The Zeta potential measurements (ζ) of as-exfoliated and functionalized (1T) MoS_2 nanosheets were performed using an Anton Paar Litesizer 500 Particle Analyzer at neutral pH (in water). Our results shows that the zeta potential for pristine MoS_2 nanosheets is -45.4±0.8 mV confirming the presence of a large excess of negative charges in the exfoliated materials. This result agrees with previous results from the literature [1]. As expected, the Zeta potential decreases after covalent functionalization because of the consumption of the extra electrons during the functionalization reaction. We found a remarkable agreement between the contact angle and the Zeta potential for the different MoS_2 membranes. More importantly the evolution of the Zeta potential closely follows the trend of polarity of the functional groups: $\zeta_{MoS_2-Acet.} > \zeta_{MoS_2-EtOH} > \zeta_{MoS_2-Met}$ (the values are presented in Table 3 below). The Zeta potential measurements suggest that the nanosheets remain partially charged after functionalization and that the density of charges can be tuned by the nature of the functional groups grafted on the nanosheets.

Supplementary Table 1 Zeta potential and contact angle measurements of as-exfoliated (1T) MoS_2 and functionalized MoS_2

Samples	Zeta potential (ξ, mV)	Contact angle
1T MoS_2	-45.4 ± 0.8	58°
2H MoS_2	-30 (Ref 6)	98°
MoS_2-Acet.	-39.3 ± 0.4	72°
MoS_2-Met.	-29.6 ± 0.3	90°
MoS_2-EtOH	-35.5 ± 0.7	80°

Contact angle measurements from single layer 2H MoS_2

The contact angle of the as-exfoliated (1T) MoS_2 membranes is 58°. We compared this value with the contact angle of single-layer 2H MoS_2 grown by chemical vapor deposition [2]. We found that the contact angle of 2H MoS_2 is ~ 95° (Supplementary Figure 2). This value is close to the ones reported by Chow et al. for single-layer MoS_2 and WS_2: 82° and 85°, respectively. The lower contact angle of as-exfoliated MoS_2 membranes is attributed to the presence of charge in chemically exfoliated 1T MoS_2. Indeed Heising et al. have reported that there is a 30% excess of charge in the chemically exfoliated MoS_2 nanosheets[4]. This is also confirmed by the Zeta potential of as-exfoliated MoS_2 which is significantly larger than that of functionalized MoS_2 and 2H MoS_2 [5]: -45.4 mV vs. -30 mV for 1T and 2H MoS_2, respectively.

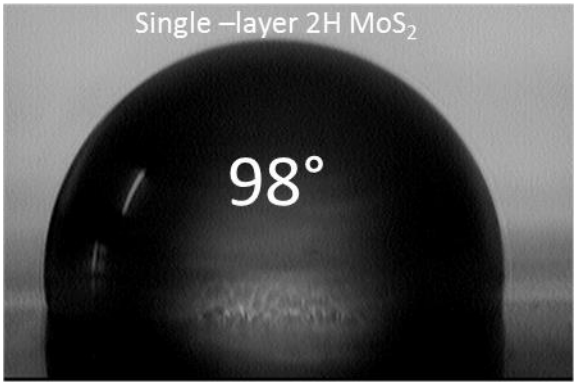

Supplementary Figure 2. Water contact angle for single-layer MoS_2 grown by CVD and deposited on SiO_2/Si wafer.

Functionalization of single-layer MoS_2 nanosheets

Single-layer MoS_2 nanosheets were functionalized using organohalide reagents. Functionalization of the nanosheets was performed either in solution or directly on the membranes. According to the (002) peak obtained from X-ray diffraction (XRD), the *d*-space is estimated to about 13 Å ($2\theta = 6.6°$) and 6.18 Å ($2\theta = 14.4°$) in the case of as-filtered and dried MoS_2 membrane respectively (Supplementary Figure 3). The large physical gaps between the MoS_2 nanosheets allow the reagents and the solvent to slowly diffuse between the layers. The reagent solution was let to slowly diffuse through the MoS_2 membrane for 48 hours after what the membrane was rinsed with 2-propanol (4×50 mL), ethanol (4×50 mL) and water (4×50 mL). The organohalide reagent is typically dissolved in the 2:1 water:2-propanol solution at the concentration of 15 mM. For example, for a membrane of 250 nm in thickness, the typical mass of MoS_2 nanosheets is estimated to be 1.14 mg (7.1×10^{-6} mol). A 10-fold excess of iodomethane corresponding to 7.1×10^{-5} mol (0.010 g) was used for the functionalization and dissolved in 4.7 mL of water:2-propanol solution. The excess of reagents and sub-products of the reaction was eliminated by rising with 2-propanol (4×50mL), ethanol (4×50 mL) and water (4×50 mL). Finally the membranes were dried in air at 60°C under atmospheric pressure. Cross section SEM observations confirm the stacking of the nanosheets in the different functionalized MoS_2 membranes while the presence of aggregates and crumpling is not detected (Supplementary Figure 5).

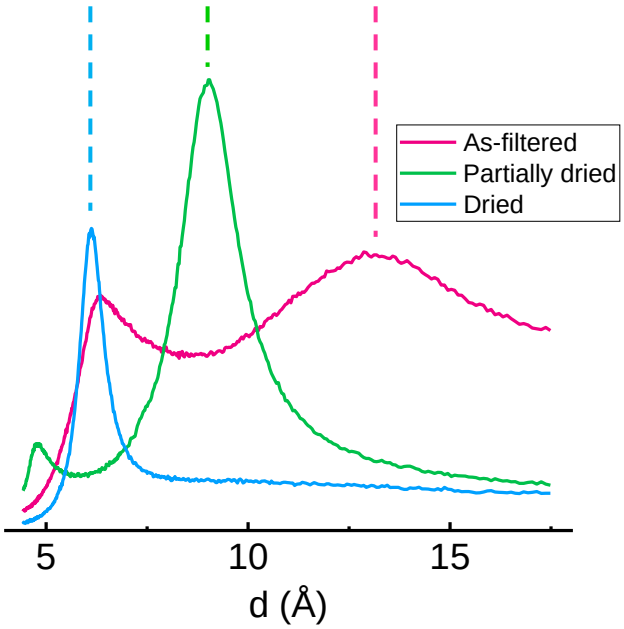

Supplementary Figure 3. X-ray diffraction spectra centered around the (002) peak (dashed line) from as-filtered (pink), partially dried (green) and dried (blue) nanolaminate MoS_2 membrane

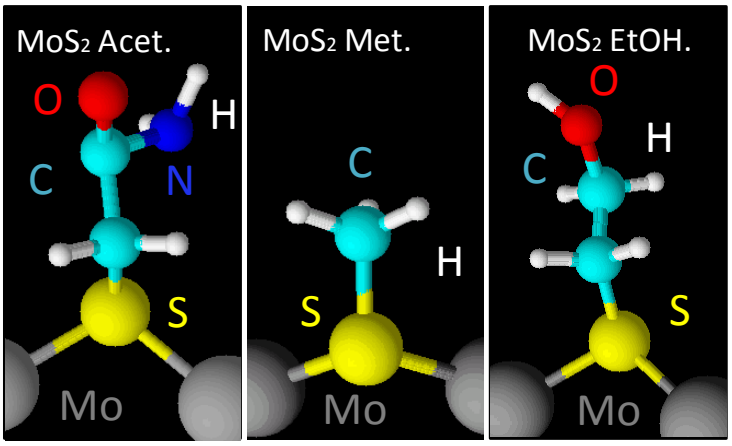

Supplementary Figure 4. Schematic representation of the functional groups on the surface of the MoS_2 nanosheets.

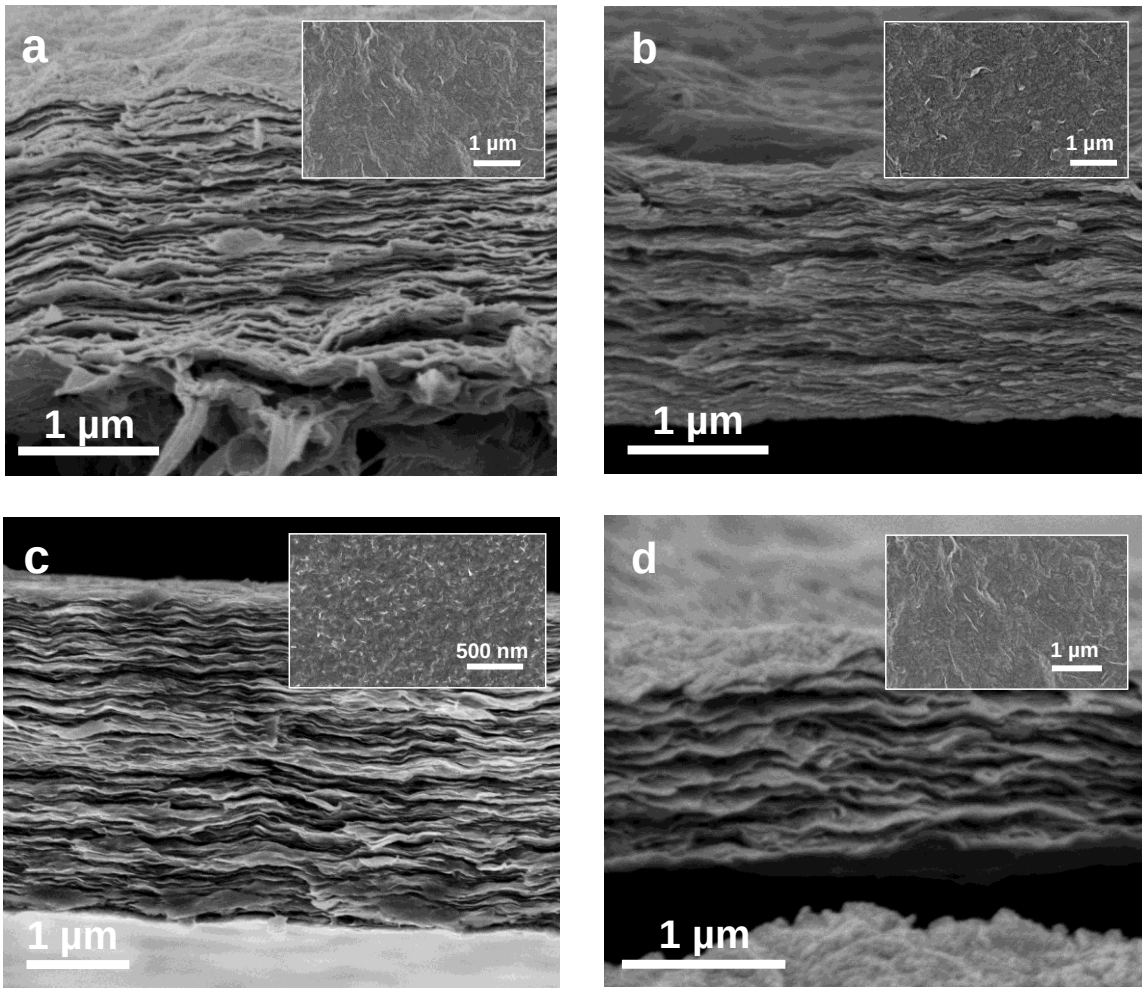

Supplementary Figure 5. Cross section images of pristine (a), acetamide (b), methyl (c) and ethyl-2-ol (d) functionalized MoS_2 membranes. Insets: Top view observations of the corresponding membranes under SEM.

To further attest the covalent bonding of functional groups on MoS_2, we let the exfoliated MoS_2 nanosheets reacting with acetamide following the same methodology. Supplementary Figure 6 shows the X-ray diffraction signals from membranes made of exfoliated MoS_2 nanosheets treated with acetamide and 2-iodoacetamide. We observe no shift of the (002) peak in comparison to non-functionalized MoS_2 membranes. This indicates that the washing step, after functionalization, efficiently removes any

intercalated species non-covalently bonded to the nanosheets. It also demonstrates the key role played by the iodine groups in the functionalization reaction.

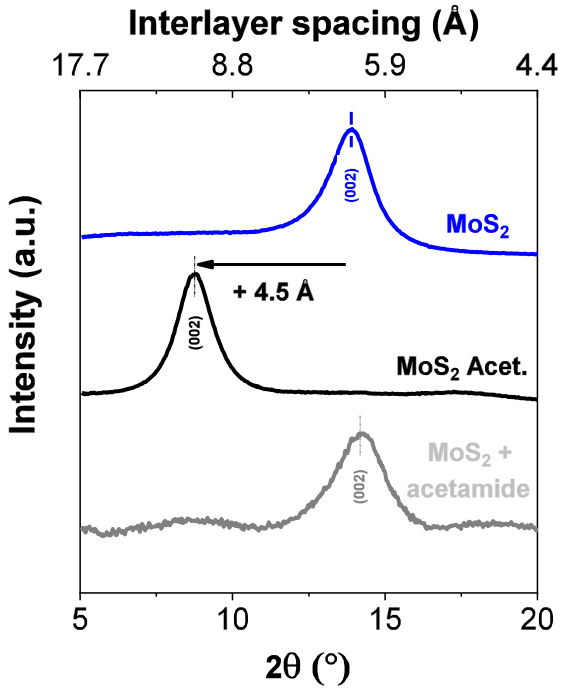

Supplementary Figure 6. X-Ray diffraction spectra from non-functionalized MoS_2 membranes compared to MoS_2 membranes treated with acetamide and 2-iodoacetamide.

Synthesis of single-layer graphene oxide (GO)

GO was prepared from natural graphite by the modified Hummers' method.[6] Graphite powder (1.5 g) was mixed with H_2SO_4 (50.7 mL) and sodium nitrate (1.14g). In an ice bath, $KMnO_4$ (6 g) was added slowly while stirring. After 72 hours, 150 mL solution of H_2SO_4 was slowly added and the reaction was finally quenched by the addition of 4.5 mL of H_2O_2 (30%). Metal ion impurities were removed by treating the solution with 10% HCl. The solution was then washed using dialysis (molecular weight cut-off = 14,000,

Sigma-Aldrich) to completely remove metal ions and acids. The GO nanosheets were centrifuged at 3,000 rpm for 3 minutes to remove the non-exfoliated particles.

Physical characterizations

X-ray photoelectron spectroscopy (XPS, Thermo Scientific K-Alpha spectrometer) was performed using a Al-Kα microfocused monochromatized source (1486.7 eV) with a resolution of 0.6 eV and a spot size of 400 μm. High resolution transmission electron microscopy images (HRTEM) were obtained using HRTEM JEOL 2200 FS microscope with an emission gun operating at 200 kV. Elemental mappings have been performed using Scanning Transmission Electron Microscope (STEM) coupled with energy dispersive X-ray spectroscopy (EDS) using SDD JEOL (30 mm^2- 129 eV). Functionalized MoS_2 nanosheets were characterized using RAMAN spectroscopy (Renishaw 1000 system operating at 514 nm), attenuated total reflectance FTIR (Nicolet Nexus FT-IR spectrometer equipped with a ATR Diamant Golden Gate) and solid state ^{13}C CP MAS NMR (Bruker Avance 700 MHz). Organohalide reagents were analyzed by ^{13}C solution nuclear magnetic resonance (Avance 300 MHz instrument from Bruker); both 2-iodoethanol and iodomethane were analyzed using $CDCl_3$ (77.3 ppm) as an internal solvent whereas 2-iodoactetamide spectra was recorded in D_2O. X-ray Diffraction was performed on an Xpert Pro apparatus (Philips Pana Analytical, Cu Kα; λ = 1.5418 Å) operating at 40 kV and 20 mA. Scanning electron microscopy (SEM) was carried out on a Zeiss Sigma Field Emission SEM with an Oxford INCA PentaFETx3 EDS system (model 8100).

ATR-FTIR spectroscopy measurements on functionalized MoS_2 membranes

ATR-FTIR spectroscopy was performed on MoS_2-derived materials (Supplementary Figure 7). The ATR-FTIR spectra of functionalized MoS_2 nanosheets bring the first evidence of covalent grafting of the functional groups. The S-C stretching is identified at ~ 710 cm^{-1} for both acetamide-, methyl- and ethyl-2-ol- functionalized MoS_2 , whereas the stretching mode γ_W for S-CH_2- appears at 1151 cm^{-1} and 1129 cm^{-1} for acetamide and ethyl-2-ol- functionalized MoS_2. The deformation modes δ for C-H are clearly visible at 1293 cm^{-1} and 954 cm^{-1} in methyl- functionalized MoS_2 [7].

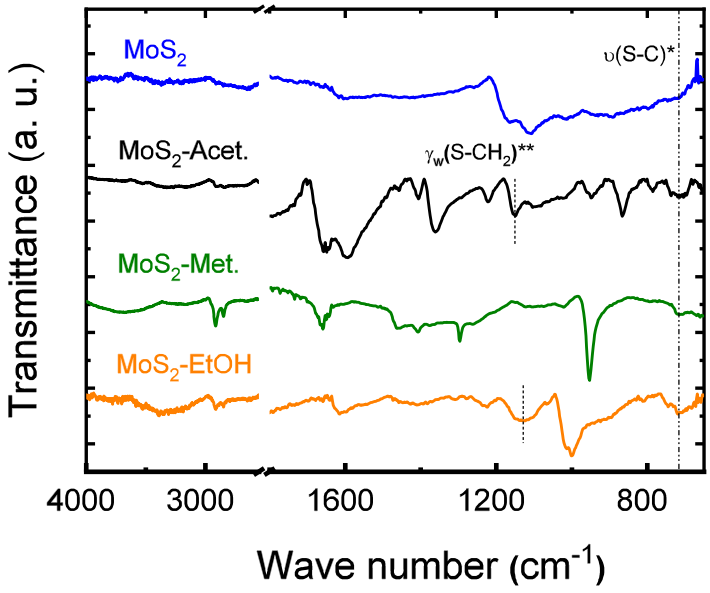

Supplementary Figure 7. ATR-FTIR spectra of pristine (non-functionalized) MoS_2 (blue), acetamide- functionalized MoS_2 (black), methyl- functionalized MoS_2 (green) and ethyl-2-ol- functionalized MoS_2 (orange); (*: [7]; **: [8]).

Acetamide- functionalized MoS_2 nanosheets have been further studied on Supplementary Figure 8 wherein ATR-FTIR spectra of pristine MoS_2 (blue trace) is compared to

acetamide- functionalized MoS_2 (black), 2-iodoacetamide (brown), and pure acetamide compound (red). Acetamide functionalized MoS_2 displays strong signals at 1655 cm^{-1} and 1605 cm^{-1} attributed to C=O and N-H stretching [7]. Remarkably the FTIR response for acetamide- functionalized MoS_2 appears very similar to acetamide.

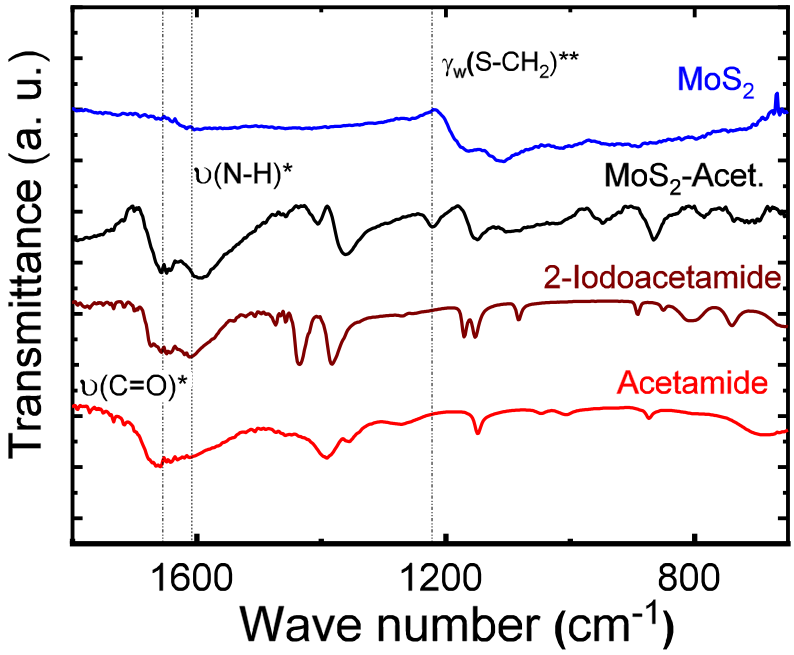

Supplementary Figure 8. ATR-FTIR spectra of pristine (non-functionalized) MoS_2 compared with covalently functionalized MoS_2 nanosheets with acetamide groups (black trace), 2-iodoacetamide (brown trace) and acetamide (red trace); (*: [7]; **:[8]).

TGA measurements on functionalized MoS_2 membranes

Thermogravimetric analysis (TGA) were performed on a TGA Q500 Thermogravimetric Analyzer equipped with Thermal Analysis Controller. After purging the system for 30 min at 50°C, samples were heated under nitrogen at 10°C-min^{-1} from 50°C up to 800 °C. The weight loss has been recorded for pristine MoS_2 and functionalized MoS_2 nanosheets

(Supplementary Figure 9a). The derivative signal from pristine MoS_2 nanosheets remains relatively flat. At the opposite, the derivative of the weight loss shows peaks at 223°C, 248° and 378°C for the degradation of ethy-2-ol, acetamide and methyl groups respectively (Supplementary Figure 9b). The extent of functionalization was calculated from the weight loss at 500°C and assuming that the difference between the weight loss from pristine and functionalized MoS_2 nanosheets is solely coming from the degradation of the grafted functions. The functionalization degrees per sulfur reach ~ 19 at.%, ~ 22 at.% and ~ 55 at.% for MoS_2-Acet., MoS_2-EtOH and MoS_2-Met. respectively. These values are in relatively good agreement with the XPS results obtained by deconvoluting the S-C signals from the S2p regions. We note that the higher functionalization degree for MoS_2-Met. is explained by the difficulty in precisely measuring the weight solely coming from the methyl groups.

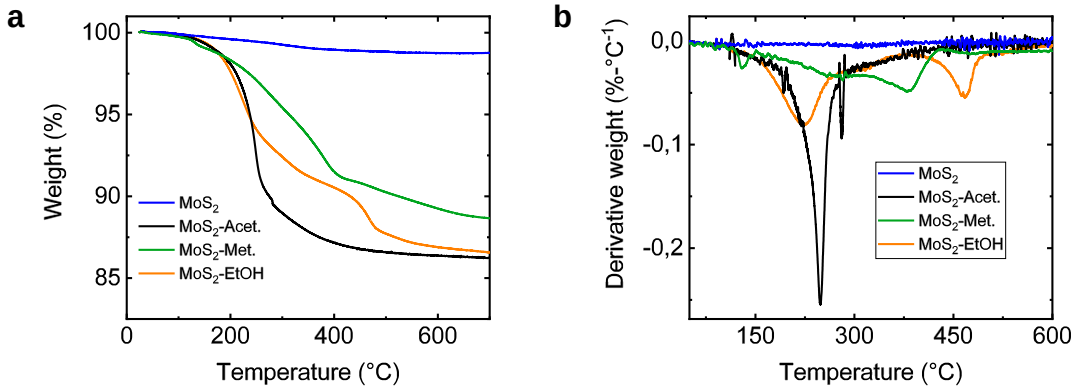

Supplementary Figure 9. (**a**) Thermogravimetric traces of pristine and functionalized MoS_2 nanosheets up to 700°C under N_2. (**b**) First derivative of the TGA traces.

^{13}C Nuclear Magnetic resonance spectroscopy (NMR)

The solid-state ^{13}C CP MAS NMR experiments were performed on a Bruker 700 MHz (16.4 T) spectrometer at a frequency of 176.05 MHz, using a 3.2 mm Bruker MAS probe (contact time: 2 ms, SPINAL-64 {^{1}H} decoupling, ramp 90 scheme during the polarization transfer, rotation frequency: 12 kHz, recycle delay: 4 s, number of scans: between 42K and 58K). The samples were prepared by mixing NaCl with the powders followed by careful packing of the mixture into a 3.2 mm zirconia rotor. ^{13}C chemical shifts were referenced to tetramethylsilane, using adamantane as a secondary reference.

To confirm the shift of the α-C after covalent attachment on the S atoms of the MoS_2 nanosheets, liquid-state ^{13}C NMR were performed on the organohalide reagents used for each functionalization route (Supplementary Figure 10). The chemical shift from O=*C*-NH_2 bond in 2-iodoacetamide, and HO-*C*H_2-CH_2 bond in 2-iodoethanol appear respectively at 174.8 ppm and 63.37 ppm. These peaks are not significantly shifted after functionalization (main Figure 2a). The chemical shift of the α-C from C-I appears at -2.51 ppm, -23.20 ppm and 8.97 ppm for 2-iodoacetamide, iodomethane and 2-iodoethanol, respectively (Supplementary Figure 10). These peaks are largely shifted by 40-50 ppm after covalent grafting on the surface of the MoS_2 nanosheets (main Figure 2a).

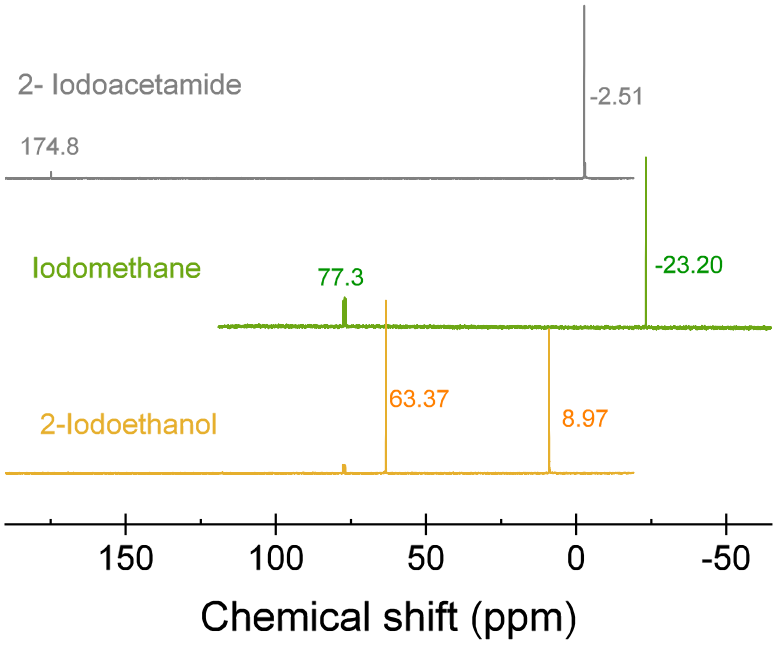

Supplementary Figure 10. Liquid-state ^{13}C NMR spectra of 2-iodoacetamide (grey), iodomethane (green), 2-iodoethanol (orange). The chemical shift observed at 77.3 ppm for 2-iodoethanol and iodomethane originates from $CDCl_3$ used as solvent.

X-ray photoelectron spectroscopy (XPS) on functionalized MoS_2 membranes

Covalent functionalization was also probed by X-ray photoelectron spectroscopy. First from the survey spectra, no iodine was detected, which confirms the successful rinsing of the MoS_2 nanosheets after the functionalization reaction (Supplementary Figure 11, left).

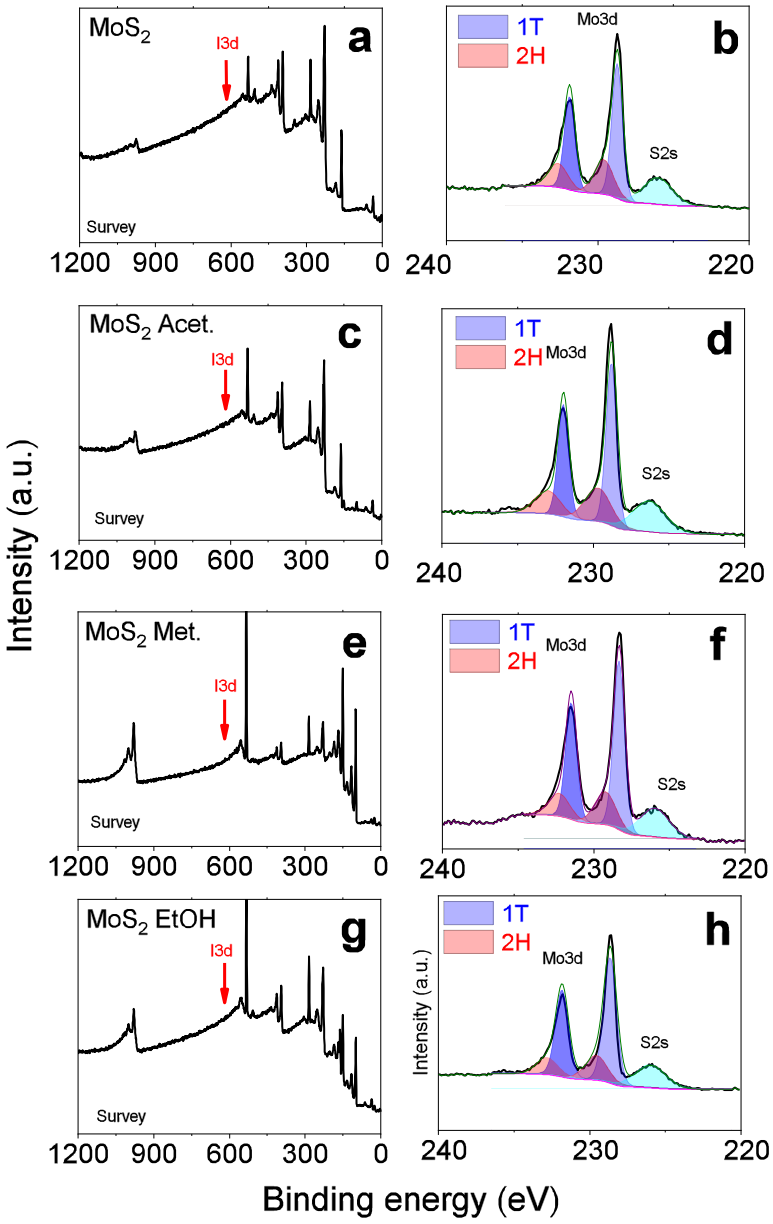

Supplementary Figure 11. XPS survey (left) and Mo3d (right) spectra from the pristine and functionalized MoS_2 nanosheets.

X-ray photoelectron spectra for the S2p and Mo3d regions are shown in Supplementary Figure 12. As reported previously in the case of chemically exfoliated MoS_2, the S2p and Mo3d regions can be convoluted with components from the 1T and 2H phases. The presence of functional groups can be seen on the S2p regions (158-166

eV) whereas signals from the Mo3d regions remain virtually unchanged (389-400 eV). Such changes are attributed to the formation of the S-C bonds (in green) due to the covalent grafting on the S atoms.

Another evidence of functionalization is brought from the N1s region in the case of the acetamide-functionalized MoS_2 (Supplementary Figure 12). For comparison, no N1s can be detected at ~ 400 eV from the pristine non-functionalized MoS_2 nanosheets. The fitting of the N1s signals enables quantification of the functional groups. The N/Mo is estimated to 40 at.% giving a functionalization degree of 20 at.% per sulfur atoms. Similar functionalization degree has been measured from S-C signals obtained by the deconvolution of the S2p signals (Supplementary Table 2).

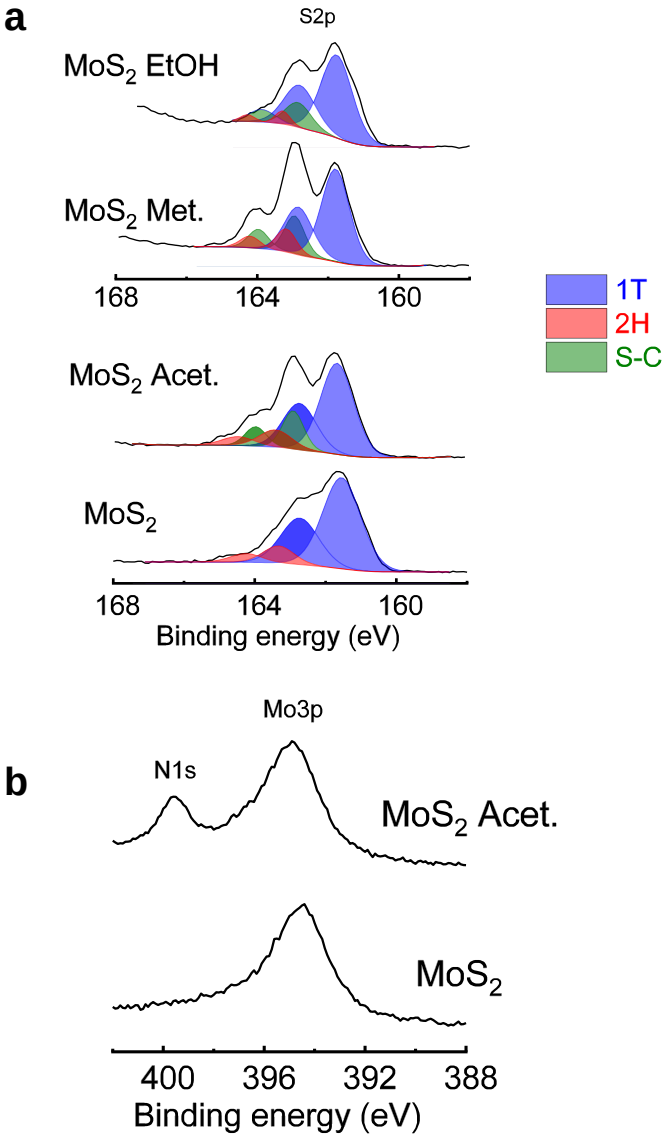

Supplementary Figure 12. X-ray photoelectron spectra of S2p (a) and N1s (b) regions from the pristine and functionalized MoS_2 nanosheets. The functionalization degree refers to the percentage of functionalization group per S atoms.

Supplementary Table 2. Details of the XPS results for MoS_2 and functionalized MoS_2 samples. The functionalization degree refers to the percentage of functionalization group per S atoms.

MoS_2-Met.					
	Peak position (eV)	**FWHM (eV)**	**Area (P) CPS**	**at.%**	**Funct. degree (%)**
1T	161.8	0.93	7817.9	62.5	
	162.9		3993.5		
2H	163.2	0.67	1595.1	12.8	
	164.2		814.8		
S-C	162.9	0.88	3091.5	24.7	25
	164.0		1579.17		
MoS_2-Acet.					
1T	161.7	1.11	6375.6	68.3	
	162.7		3256.7		
2H	163.4	1.08	1186.3	12.7	
	164.5		605.9		
S-C	162.9	0.70	1767.2	19	19
	164.0		899.8		
MoS_2-EthOH					
1T	161.65	1.05	5715.3	75.8	
	162.7		2919.4		
2H	163.18	0.48	416.8	5.5	
	164.18		212.9		
S-C	162.75	0.87	1406.9	18.7	19
	163.77		718.7		

Raman spectroscopy on functionalized MoS_2 nanosheets

1T phase of MoS_2 has two Raman modes, the in-plane mode E^1_{2G} and the out-of-plane mode A_{1G}, as well as J_1, J_2 and J_3 vibrational modes recently identified by Calandra [9]. Supplementary Figure 13 shows the Raman spectra of MoS_2-derived materials where

only a weak signal of the E^1_{2G} mode is observed for pristine MoS_2 (blue trace); indicating a majority of 1T-phase MoS_2. In accordance with the literature, J_1, J_2 and J_3 vibrational modes are observed at 147 cm^{-1}, 236 cm^{-1}, and 332 cm^{-1}. As previously reported by Voiry et al. [7], the signal from the 1T phase is preserved after functionalization. The A_{1G} band splits into two signals due to the covalent binding on the S atom. Both J_1 and J_3 widen and get downshifted whereas J_2 peak gets significantly stronger and upshifted. In addition, strong bands attributed to the anchorage of molecules on the nanosheets can be detected. New peaks appear at ~ 260 cm^{-1} and at ~ 320 cm^{-1} for all the functionalized samples clearly indicating new vibrational modes due to the covalent attachment on the sulfur atoms. A new peak is also detected at ~ 210 cm^{-1} for both acetamide- and methyl-functionalized MoS_2.

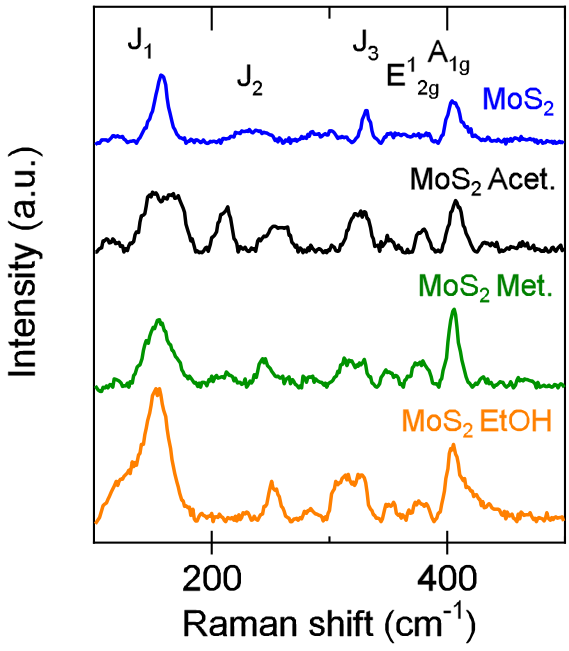

Supplementary Figure 13. Raman spectra of pristine (non-functionalized) MoS_2 (blue), acetamide-functionalized MoS_2 (black), methyl-functionalized MoS_2 (green) and ethyl-2-ol-functionalized MoS_2 (orange).

X-Ray diffraction (XRD) on MoS_2 membranes

The d-spacing between the MoS_2 layers can be precisely measured using X-ray diffraction (main Figure 2b-d). Upon lithium intercalation, the d-spacing increases from $2\theta = 14.4°$ up to ~ 7.6° due to the presence of hydrated Li cations (Supplementary Figure 14). After exfoliation and removing Li cations *via* centrifugation, the d-spacing in the restacked MoS_2 reaches $2\theta = 13.96°$. Such a minor change in the d-spacing combined to the relative high intensity of the (002) peak suggests a high degree of alignment of the nanosheets in the membranes.

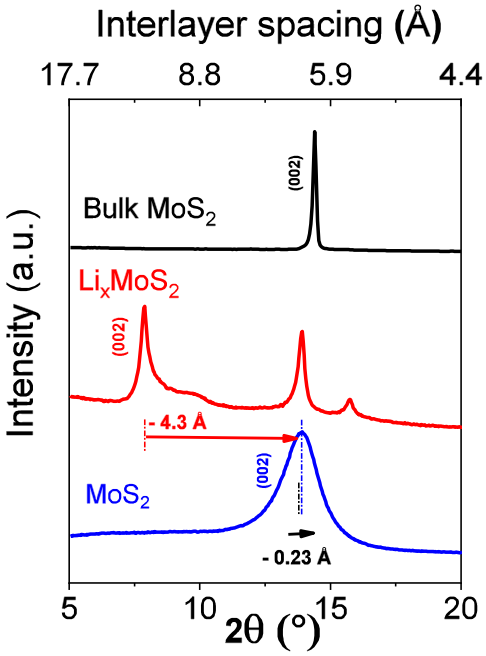

Supplementary Figure 14. X-Ray diffraction spectra from bulk 2H-MoS_2 crystal (black), lithium intercalated MoS_2 obtained while liquid exfoliation (red) and pristine non-functionalized MoS_2 membrane (blue).

Interlayer spacing of membranes *d* are summarized in Supplementary Table 3. and were determined using XRD measurements for all the functionalized MoS_2 membranes (see the corresponding diffractograms in main Figure 2b). The full width at half maximum (FWHMs) of (002) peak are similarly sensitive within all functionalized structures suggesting a comparable degree of functionalization. Interestingly slightly larger *d*-spacing are measured for methyl-functionalized MoS_2 membranes. This is surprising as methyl functions are smaller compared to ethyl-2-ol and acetamide (see Supplementary Table 3) suggesting different arrangements of the functional groups in the capillaries depending on their size and polarity.

The pore spacing (or capillary width) was estimated by the difference between the interlayer d spacing measured from XRD and the thickness of a single-layer of MoS_2: 6.15 Å (c/2, with c the lattice parameter of 2H MoS_2). Our approach is thus similar to previous work from Abraham et al. on graphene oxide [10]. Using molecular dynamic simulations, we report water density profiles in the direction perpendicular to the flux inside 2D channels of 12 Å separation (Supplementary Figure 15). Our molecular dynamic results show that water molecules do not get closer to sulfur atoms than 1.45 Å giving a hydrodynamic thickness of 5.57 Å. The space that is inaccessible to water molecules is estimated to be: 12-5.57 = 6.43 Å – close to the 6.15 Å used for the study.

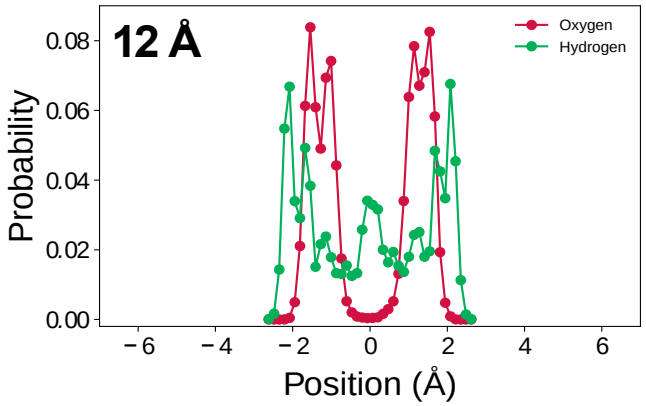

Supplementary Figure 15. Water density profile for O and H along the Y-direction for pristine MoS_2 nanochannel with a 12 Å separation.

Supplementary Table 3. Comparison of lamellar structures of GO and MoS_2 derived membranes. Capillary width of GO and MoS_2-based membranes were estimated by considering the thickness of pristine graphene and MoS_2 nanosheets: 3.4 Å and 6.15 Å respectively [8]. Errors correspond to standard deviation between several samples.

Samples	Interlayer spacing d (Å)	Average FWHM of (002) peak	Capillary width δ (Å)*
Graphite	3.4	-	-
GO	8.3 (± 0.07)	0.3	4.9
Bulk MoS_2 powder	6.14	-	-
Exfoliated MoS_2	6.18 (± 0.03)	1.35	0.035
MoS_2-Acet.	10.1 (± 0.07)	0.6	3.93
MoS_2-Met.	11.5 (± 0.02)	0.82	5.37
MoS_2-EtOH	10.8 (± 0.04)	0.64	4.69

Stability of the functionalized MoS_2 membranes

Graphene oxide membranes are typically found unstable in water due to uncontrollable swelling. In order to assess the stability of the MoS_2 membranes, the

membranes were soaked in water for a period of one month. No visible macroscopic degradations are visible on the membranes as shown in Supplementary Figure 16.

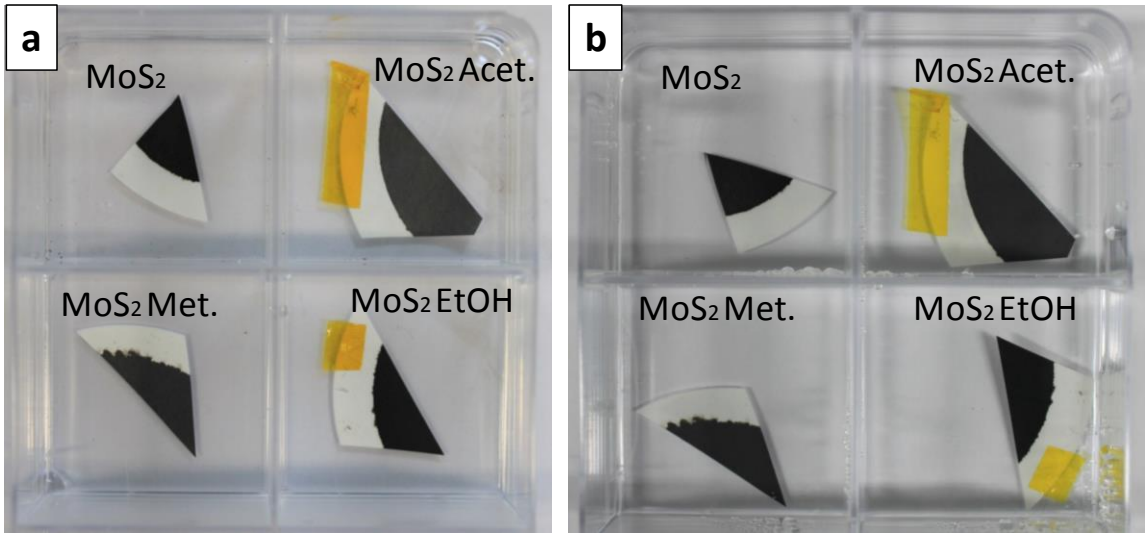

Supplementary Figure 16. Pictures of pristine and functionalized MoS_2 membranes before (a) and after several months in DI water (b).

Controlled of the swelling in the functionalized MoS_2-based membranes

In order to confirm the absence of deformation of the MoS_2 membranes, the interlayer spacing was measured using X-ray diffraction after soaking the membrane in DI water. Supplementary Figure 17 shows the diffractograms of the MoS_2 membranes compared to graphene oxide membranes for different soaking times.

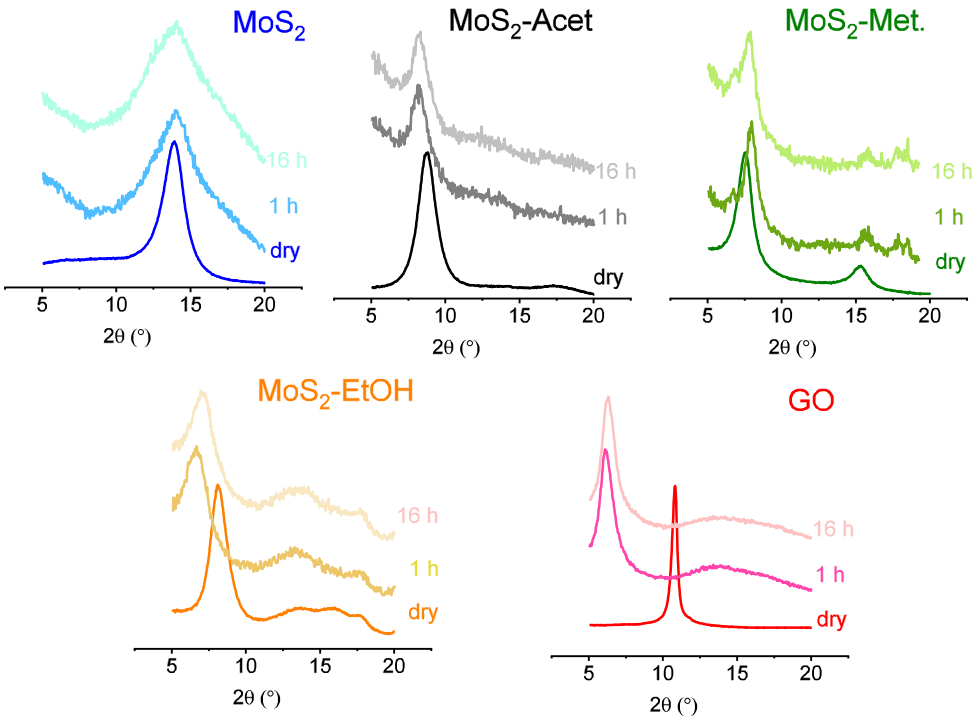

Supplementary Figure 17. X-ray diffraction spectra of 1µm thick MoS_2 membranes dried and after 1 hour and 16 hours.

Next we investigated the consequences of hydration of the membrane on the (002) of the methyl- functionalized MoS_2 membranes with different thicknesses. Supplementary Figure 18 shows the XRD spectra of MoS_2-Met. membranes after 1h, 6h and 48 h soaked in water. Our results show that the MoS_2-Met. membranes do not swell and the broadening of the (002) peak is virtually not affected. We attributed this phenomenon to the hydrophobic nature of methyl groups.

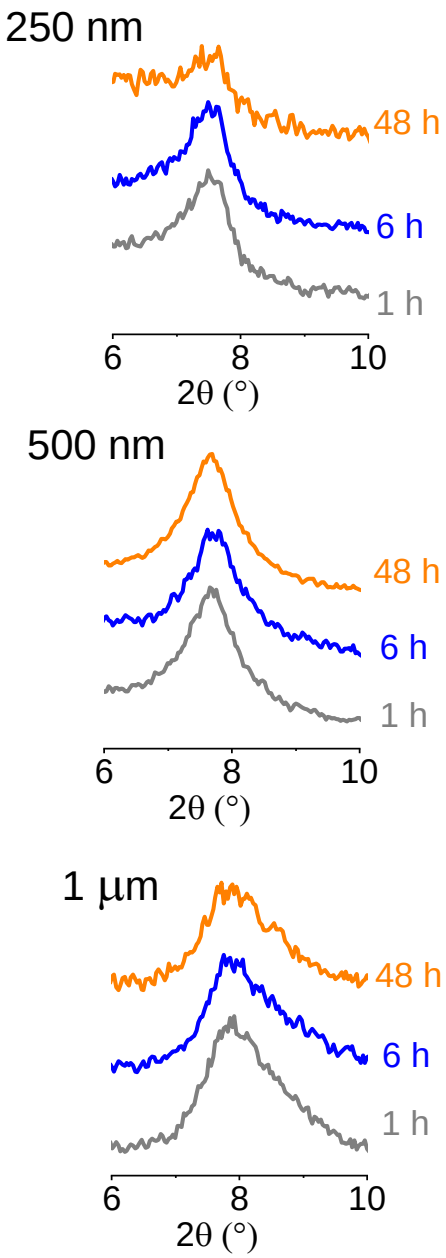

Supplementary Figure 18: X-ray diffraction spectra from hydrated MoS_2-Met. membrane soaked in water for 1h, 6h and 48 h.

Ion permeance measurements

As discussed in the main text, ionic sieving properties have been examined. The ionic species tested in this work include NaCl, LiCl and KCl. We note that the anion is the same for all the salts so that the difference between the ion permeation rates is assumed to be solely due to cations. Ion permeation rate measurements were carried out in two Teflon-made compartments using 500 nm-thick membranes and the 2 compartments were covered with aluminum foil in order to prevent water evaporation. Both permeate and feed reservoirs were filled with the same volume of 200 mL of DI water and aqueous ionic solution respectively (Supplementary Figure 19a). Ion transportation has been measured by recording the conductivity of the permeate solution over several hours. The size of the membrane was typically 1 cm^2 in order to test at least 4 membranes from the same batch. To assess the transport properties, we performed the measurements for different ionic strengths corresponding to salt concentration of 0.25 M, 0.625 M and 1 M in the feed side. As an example, Supplementary Figure 19b shows the permeation of NaCl across both acetamide- and ethyl-2-ol- functionalized MoS_2 membranes using 1 M of NaCl as feed compartment.

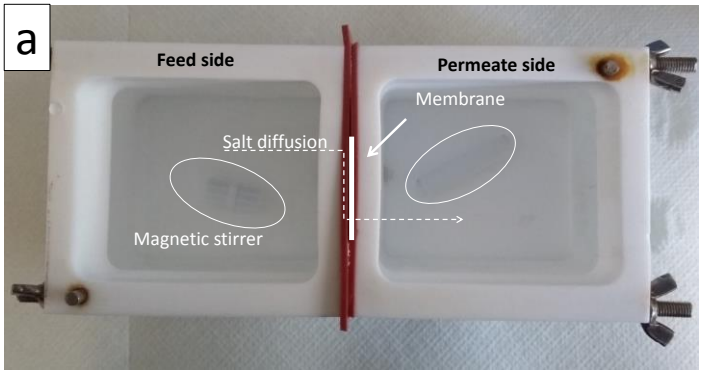

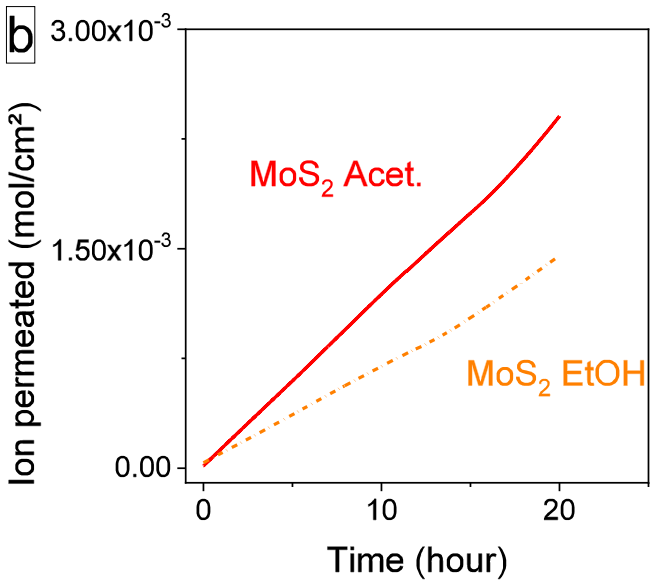

Supplementary Figure 19. Cell used for the conductivity measurement consisting of two compartments with the feed and permeate solutions **(a)** and evolution of the ion permeation across acetamide- (red line) and ethyl-2-ol- (orange line) functionalized membranes using a 1 M NaCl aqueous solution as feed solution **(b)**.

The impact of the functional groups on the sieving mechanisms of several salts have been further investigated (Supplementary Figure 20). Hydrated ion diameters corresponding to cations only were obtained from Ref [10]: 6.6 Å, 7.1 Å and 7.6 Å for K^+, Na^+, and Li^+ respectively. In the case of acetamide- functionalized membranes, ion permeance rates do not significantly change for all tested species at concentrations of 0.25 M and 0.625 M. Overall the salt diffusion for small monovalent ions across acetamide-functionalized MoS_2 membranes is rather independent of the size of the ions. The situation is different in the case of ethyl-2-ol-functionalized membranes, for which the ion permeance rate appears to be more controlled by the size of the ions (for concentrations $\geq$ 0.625 M) as previously seen in the case of graphene oxide membranes[16]**.** This result further demonstrates the influence of the surface chemistry for tuning the

ionic diffusion in the 2D nanocapillaries.

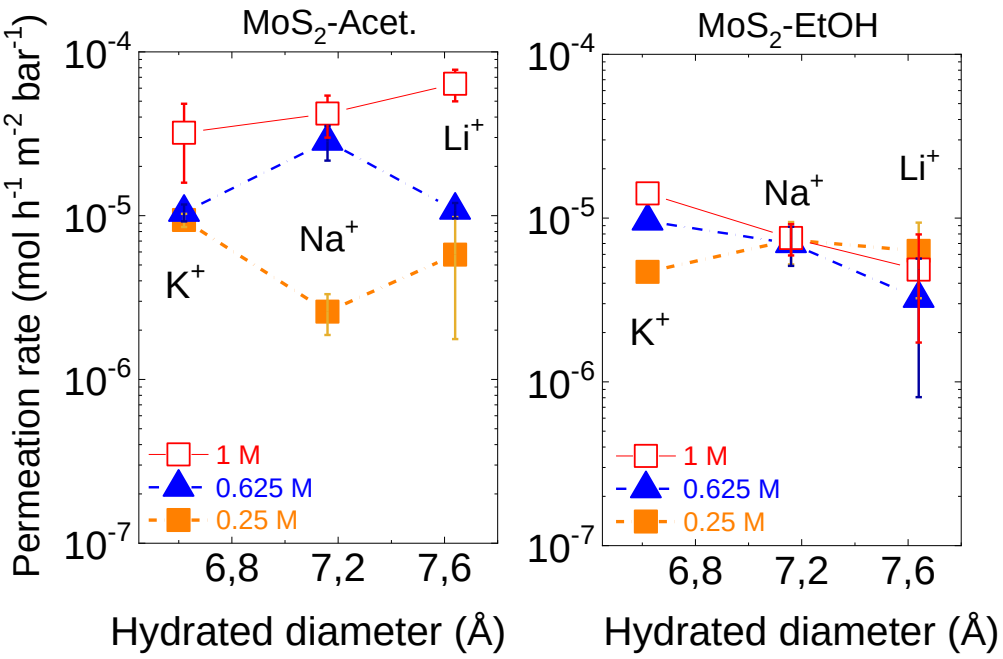

Supplementary Figure 20. Permeation rates of Na^+, Li^+ and K^+ across acetamide-functionalized (left) and ethyl-2-ol- functionalized (right) MoS_2 membranes measured at different ionic strengths. Chloride was used as counter ion in all the cases.

Permeation rate calculations

Classical law of diffusion allows estimating the permeation rate of ions within the nanochannels. We assume that capillaries width of the structures allow the diffusion of all tested species without considering their hydrated diameters as a limiting factor. The permeation rate J is given by Equation *(1)*:

$$J = \frac{D \times \Delta C \times A_{eff}}{L_{eff}} \quad (1)$$

where D is the diffusion coefficient for ions in water ($D \approx 10^{-5}$ cm²/s for small ions [11]), ΔC is the concentration gradient, A_{eff} is the total cross-sectional area of nanochannels

and L_{eff} the diffusion length through the MoS_2-based membranes. For a 1 µm thick membrane with an area of 1 cm², the effective area through which the diffusion can occur, the ionic permeation rates can be obtained using *Equations (2,3);*

$$A_{eff} \approx 1\ cm^2 \times \frac{d}{L} \quad (2)$$

$$L_{eff} \approx L \times \frac{h}{d} \quad (3)$$

where L is the average lateral length of functionalized MoS_2 sheets (≈ 340 nm) [12].

Supplementary Table 4. Estimation of fluxes of small ions using the classical law of diffusion (considering 1 M concentration gradient).

Membrane	**A_{eff} (mm²)**	**L_{eff} (mm)**	**$J \times 10^{-4}$ (mol.h^{-1}.m^{-2}.bar^{-1})**
MoS_2-Acet.	0.36	0.28	3.15
MoS_2-EtOH	0.36	0.28	3.21

Binding energy between the ions and the functional groups

As the capillary width is typically lower than the hydrated diameters of the ions, the ions must – at least partially - dehydrate to permeate the membrane. The ion permeation for ethyl-2-ol- functionalized MoS_2 membranes increases with the decrease of the dehydration energy (Supplementary Figure 21a). The binding energy between the ions and the functional groups has been estimated using DFT calculations (Supplementary Table 5). We define the binding energy as the energy of the ion adsorbed on the functional group minus the energy of the functional group minus the energy of the ion. We found that the ions do not adsorbed on the NH_2 site of the acetamide group but rather

move to the O-site after geometry optimization. In the case of ethyl-2-ol group, the ions adsorbed on both O-site and CH_2, although the energy of the latter is relatively small. DFT calculations were performed with ORCA [13] at the B3LYP level and with the def2-TZVP basis set.

Supplementary Table 5. Binding energy between Na^+, Li^+, K^+ and Cl^- and the different functional groups.

	BE (eV)			
Ions	**Acet. (-O site)**	**EtOH (-CH_2 site)**	**EtOH(-O sites)**	**Met.**
Li^+	-2.42	-0.44	-1.8	-0.53
Na^+	-1.72	-0.19	-1.25	-0.3
K^+	-1.27	-0.04	-0.87	-0.15
Cl^-	-1.09	-0.35	n/a	-0.18

Our results demonstrate that Li^+ has a stronger affinity with acetamide and ethy-2-ol functions than Na^+ and K^+ and the interaction sites are located at the oxygen sites of the amide and alcohol groups, respectively. Supplementary Figure 21 show the permeation rates for acetamide and ethyl-2-ol- functionalized MoS_2 membranes as function of the binding energy (Supplementary Table 5). One can see that the behavior of the functionalized MoS_2 membranes depends on the nature of the functional groups. In the case of MoS_2-EtOH membranes, we found that the permeation rates increase for lower values of the binding energy, suggesting that the electrostatic interactions between the ions and the functional groups play an important role on the controlled diffusion of ions across the membrane: the weaker the interactions, the higher the ion permeation rates

(Supplementary Figure 21c). This is also supported by our Zeta potential measurements that reveal that the MoS_2 nanosheets are charged (Supplementary Table 1). The ion transport mechanism in functionalized MoS_2 membranes is thus similar to previously reported mechanism for the permeation of ions in graphene oxide membranes, where the ion permeation is also controlled by the electrostatic interactions with the charges carried by the nanosheets [14]. On the contrary, in the case of membranes made of acetamide-functionalized MoS_2 nanosheets, the permeation rates appear to mainly depend on the ionic strength (Supplementary Figure 20 and main Figure 3a), whereas the binding energy and the dehydration energy do not seem to significantly influence the ion diffusion in the nanolaminate membranes (Supplementary Figure 21). The apparent different behavior between MoS_2-EtOH and MoS_2-Acet. membranes is attributed to the reduced capillary width: 4.6 Å for MoS_2-EtOH compared to 3.9 Å for MoS_2-Acet. and the larger binding energy between the ions and the acetamide functional group. The larger capillary widths of MoS_2-EtOH membranes allow faster diffusion of the ions and thus the interactions between the ions and functional groups are likely to play a more important role on the ion permeation. At the oppostite, the ion permeation is strictly controlled by the narrower capillary width of MoS_2-Acet. and the permeation is influenced by the ionic strength of the solution.

Supplementary Table 6. Summary of the hydrated diameter, binding energy between Na^+, Li^+ and K^+ and the different functional groups compared with the permeation rates measured at 0.625M. The dehydration energies are obtained from Ref. **[15]**.

Ions	diam (Å)	Hydr. diam. (Å)	Hydr. E (eV)	BE (eV)		Permeation rates	
				Acet.	EtOH	Acet.	EtOH

Li^+	1.36	7.6	5.38	-2.42	-1.8	1.07×10^{-5}	3.23×10^{-6}
Na^+	1.9	7.1	4.24	-1.72	-1.25	2.84×10^{-5}	6.98×10^{-6}
K^+	2.66	6.6	3.34	-1.27	-0.87	1.04×10^{-5}	9.58×10^{-6}

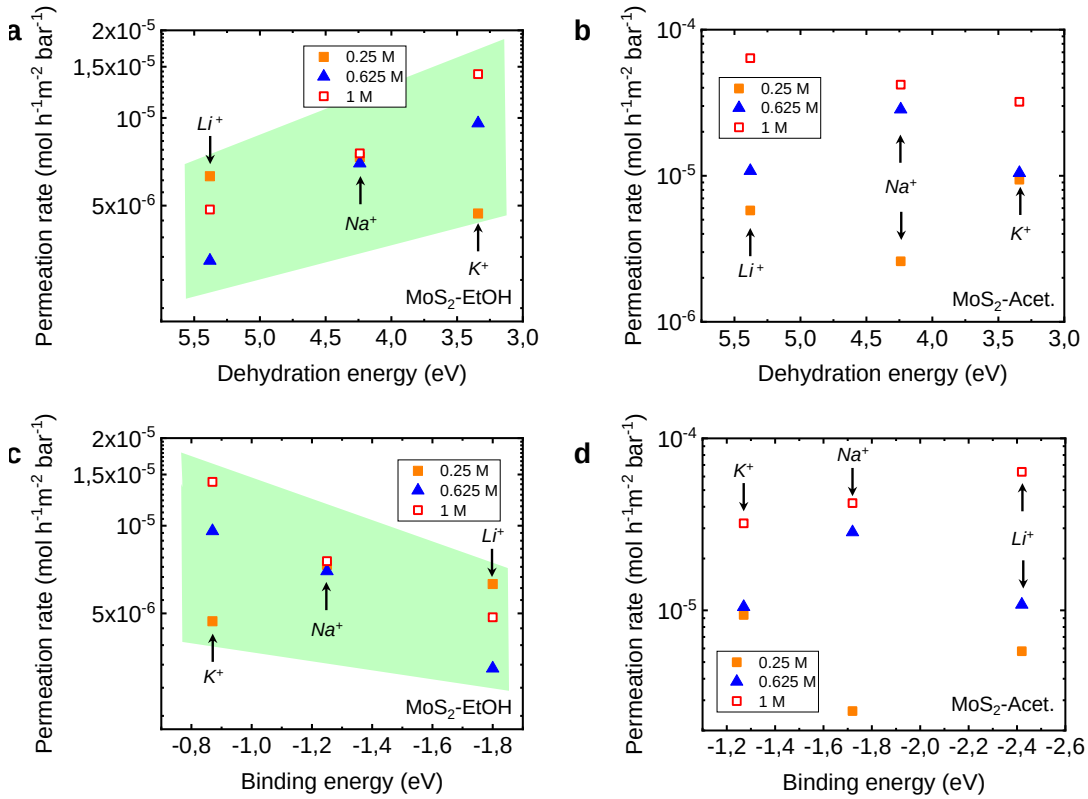

Supplementary Figure 21. Evolution of the permeation rates for MoS_2-EtOH and MoS_2-Acet. measured in forward osmosis configuration with the dehydration energy (**a,b**) and the binding energy (**c,d**) for Na^+, Li^+, K^+ and Cl^- with ionic strengths of 0.25 M; 0.625 M and 1M.

Forward osmosis (FO)-driven measurements

Water flux across the MoS_2 membranes has also been evaluated in forward osmosis configuration. Measurements have been performed using a custom-made cell presented in Supplementary Figure 22, wherein membranes were clamped between a feed and a draw glass reservoirs filled with 0.1 M NaCl and 3M KCl solution in order to generate forward

osmosis pressure of ~ 148 bar. The size of the membrane was typically 1 cm^2 in order to test at least 4 membranes from the same batch. We also fabricated and tested MoS_2 membranes from different batches to confirm the reproducibility of the results. All the membranes were tested using Nylon as porous substrate with 220-nm pore size. The water flux was directly measured from the increase of the water meniscus in the cell (yellow arrows in Supplementary Figure 22). The detection limit of the set-up is approximated to 0.01 $L.h^{-1}.m^{-2}.bar^{-1}$ considering our experimental conditions. Interestingly methyl- functionalized MoS_2 membranes do not show any water flow under forward osmosis. The suppression of the water permeance in forward osmosis in the case of methyl- functionalized MoS_2 is attributed to the hydrophobic nature of the nanosheets that does not allow water to penetrate the 2D capillaries unless sufficient external pressure is supplied to the system[16]. These membranes are thus not discussed in the following section.

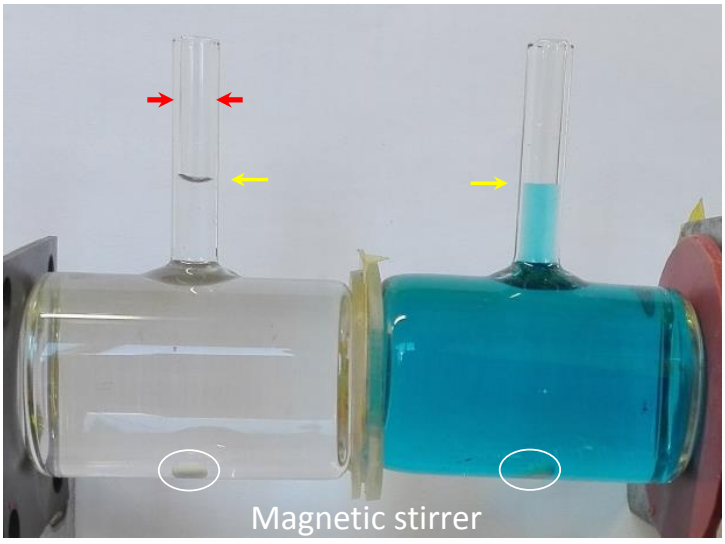

Supplementary Figure 22. Custom-made cell used for the forward osmosis measurements with the feed and draw reservoir containing the Ni-phtalocyanine solution

(right) and the 3 M KCl draw solution (left) respectively. The water meniscuses in both compartments are shown with the yellow arrows. The red arrows indicate the 5 mm-diameter cylinders used for measuring the water diffusion.

Supplementary Figure 23 presents the water flow rates obtained *via* osmosis-driven pressure for the different functionalized MoS_2 membranes. We found that water cannot permeate in the non-functionalized MoS_2 membranes in perfect agreement with the reversed osmosis results. Ethyl-2-ol- functionalized MoS_2 membranes display the highest water permeance compared to the acetamide- functionalized MoS_2 membranes. The permeance is also larger than previous results from the literature for membranes made of exfoliated-restacked nanosheets. Interestingly methyl- functionalized MoS_2 membranes do not show any water flow under forward osmosis. The suppression of the water permeance in forward osmosis in the case of methyl- functionalized MoS_2 is attributed to the hydrophobic nature of the nanosheets that does not allow water to penetrate the 2D capillaries unless sufficient external pressure is supplied to the system.

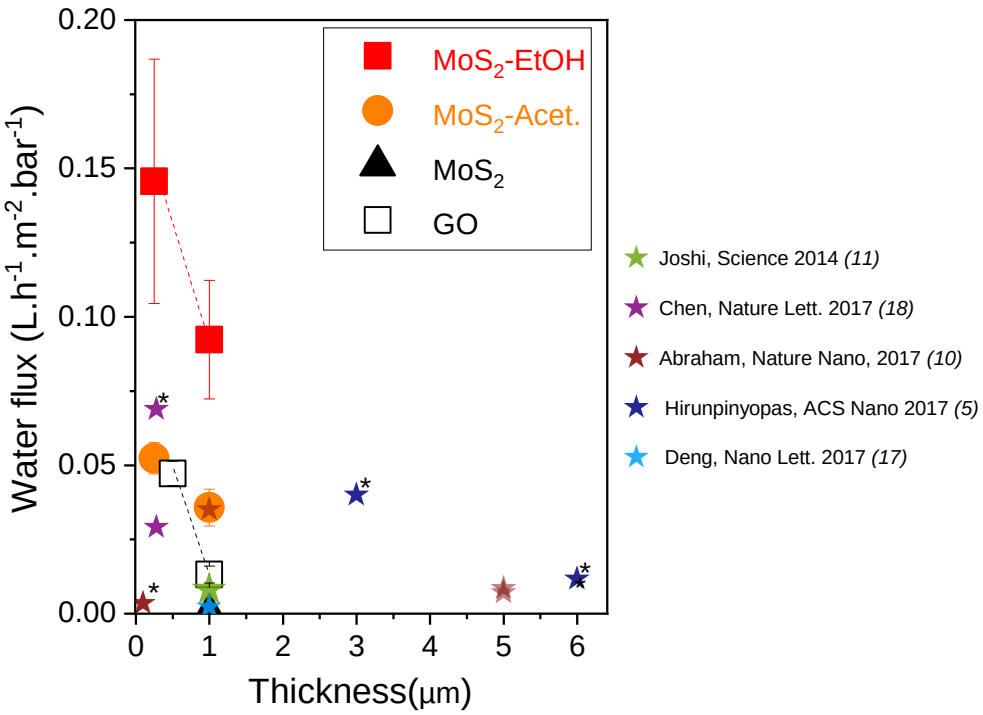

Supplementary Figure 23. Water permeance performances of several 2D-based membranes using osmotically-driven pressure. Water flow for the functionalized MoS_2 membranes is compared with the performance of graphene oxide membranes prepared at the laboratory (open squares) and references from the literature (stars) [5,10,11,17,18]

Reverse osmosis (RO) measurements

The performances of the membranes towards water permeance were characterized by measuring the amount of water crossing the membranes under increasing pressure. The different membranes have been tested using a polysulfone cell (Amicon©) in dead-end configuration under pressures up to 4 bars. The size of the membrane was typically 1 cm^2 in order to test at least 4 membranes from the same batch. We also fabricated and tested MoS_2 membranes from different batches in order to confirm the reproducibility of the results. Prior any measurements, the flow of water across the membranes was stabilized

under 4 bars for 1h. Typical water flux profile under increasing pressure is depicted in Supplementary Figure 24. The linear fit allows determining water flux (in L m^{-2} h^{-1} bar^{-1}) of membranes (main Figure 3c).

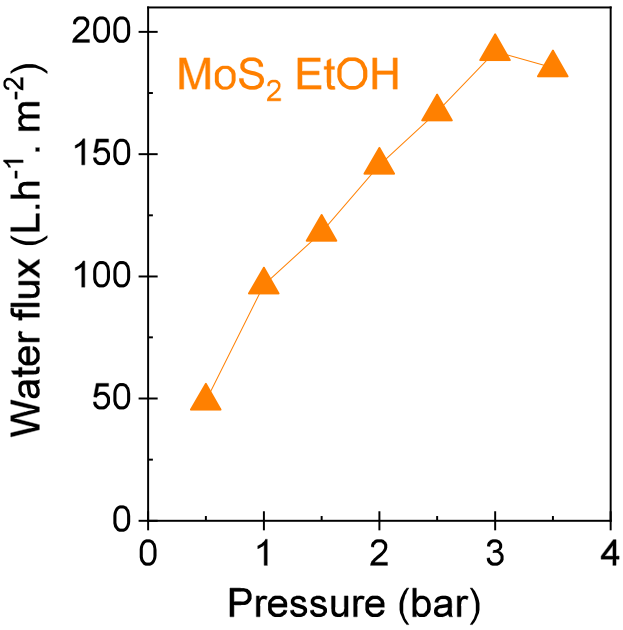

Supplementary Figure 24. Typical water flux profile obtained for ethyl-2-ol-functionalized MoS_2 membranes with a thickness 250 nm.

Interestingly the high water flux across methyl- functionalized MoS_2 membranes is maintained when increasing the thickness up to 4 µm. Supplementary Figure 25 shows the trend of water flux with thickness in methyl- and ethyl-2-ol- functionalized MoS_2 membranes. The inset shows the comparison between the water fluxes for MoS_2-Met. and MoS_2-EtOH membranes up to 2 µm in thickness. According to our molecular dynamic simulations (Supplementary Figure 43), the functionalization degree affects the water flux however, the few percent differences in functionalization degrees measured by XPS for the MoS_2-Met. cannot explain the untypical water flux of the membrane with

increased thickness (Supplementary Figure 27.b). By contrast, the distribution of *d*-spacing within the membrane can largely affect the water flux as suggested by the simulations performed on pristine membranes (Figure 4b in the main text) for which a 2 Å variation in d-spacing results (from 10 Å to 12 Å) in a 10-fold increase of the water flux. The larger FWHM of the (002) XRD peak for MoS_2-Met. compared to MoS_2-Acet. may lead to larger water flux due to different stacking order of the nanosheets (Supplementary Figure 28). We believe that this last point combined with the hydrophobic nature of the methyl group is at the origin of the behavior of MoS_2-Met. membranes compared to the MoS_2-Acet and MoS_2-EtOH membranes. The hydrophobicity of the methyl-functionalized MoS_2 membranes also translates into nanocapillaries with larger slip length. The role of the hydrophobicity on the water flux has been previously identified in the case of carbon nanotubes, whose predicted water fluxes do not depend on the length of the tube [19]. We note that the similar behavior has been reported by Hirunpinyopas et al. for dye-decorated MoS_2 membranes with a ~ 9-fold increase when the thickness increases from 1 to 6 µm and attributed to the hydrophobic surface of MoS_2 ([5]). In the case of more hydrophilic membranes such as acetamide and ethyl-2-ol membranes, the water flux rapidly decreases as the thickness increases. We suspect compaction of the thinnest MoS_2-Met.membrane because of the small size of the functional groups. The stiffness of the membrane should be explored in a follow-up study. .

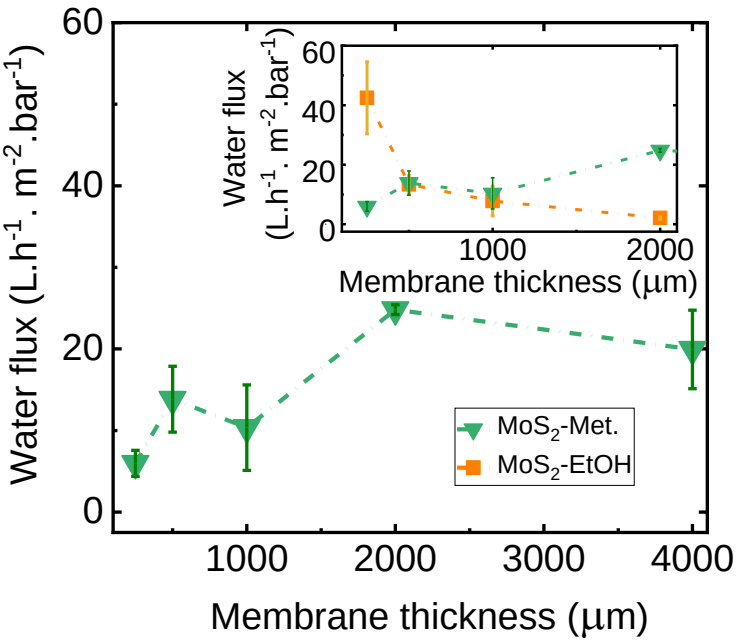

Supplementary Figure 25. Water flux for methyl-functionalized MoS_2 membranes with thicknesses up to 4 µm. Inset: Comparison water flux in thick methyl- and ethyl-2-ol-functionalized MoS_2 membranes.

Stability of the water flux in dead-end configuration

The stability of nanolaminate membranes is an important parameter and instability is typically observed for graphene oxide membranes. For example Chong et al.[13] recently showed that the water flux for graphene oxide membranes decreases from 10's L m^{-2} h^{-1} bar^{-1} to 0.1 L m^{-2} h^{-1} bar ^{1} after only 30 min. We investigated the stability of methyl-functionalized MoS_2 in dead-end configuration under a pressure of 4 bar for 15 hours. Supplementary Figure 26 shows that the water flux is largely preserved suggesting that the compaction effect is significantly reduced compared to graphene oxide membranes.

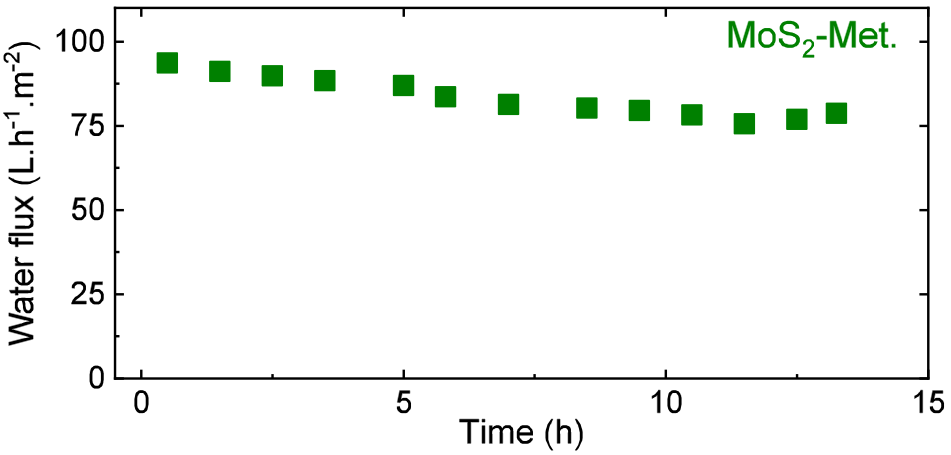

Supplementary Figure 26. Stability of the water flux for 500 nm-thick methyl-functionalized MoS_2 membrane in dead-end configuration with an applied pressure of 4 bar.

Influence of the membrane thickness on the functionalization degree and stacking order of the MoS_2 nanosheets

The influence of the thickness on the structure of the functionalized MoS_2 membranes were further analyzed using X-ray diffraction (XRD) and X-ray photoelectron spectroscopy (XPS). We first quantified the functionalization degree of MoS_2-Met. and MoS_2-Acet. membranes with different thicknesses using XPS. We note that MoS_2-Met. membranes were prepared *via* direct functionalization on the porous support whereas MoS_2-acet. and MoS_2-EtOH membranes were functionalized in solution prior filtration. The functionalization degrees of MoS_2-acet. and MoS_2-EtOH membranes are thus likely to be homogeneous. We quantified the extent of functional groups on the MoS_2-Met. nanosheets at different membrane thicknesses. To do so, XPS was performed on the core of 4 different MoS_2-Met. membranes with increasing thicknesses from 250 nm up to 2000 nm (). The XPS samples were prepared by mechanically pealing the membranes

using adhesive tape. We deconvoluted the signals from the S2p region of each sample following the same method as described above (and Table 2). The signals of the S2p doublet ascribed to the S-C bond were used to quantify the functionalization degree. Our results show that the extent of functionalization per S atom does not significantly change when increasing the thickness of the membranes. The nanosheets are slightly more functionalized on the top surface compared to the core of the membrane and the functionalization degree varies from ≈ 25% down to ≈ 19% for the top surface and the 2000 nm-thick membrane respectively. Importantly our measurements also reveal that the amount of grafted functional groups on the MoS_2 nanosheets inside the membrane remains virtually constant for thicknesses as high as 2000 nm.

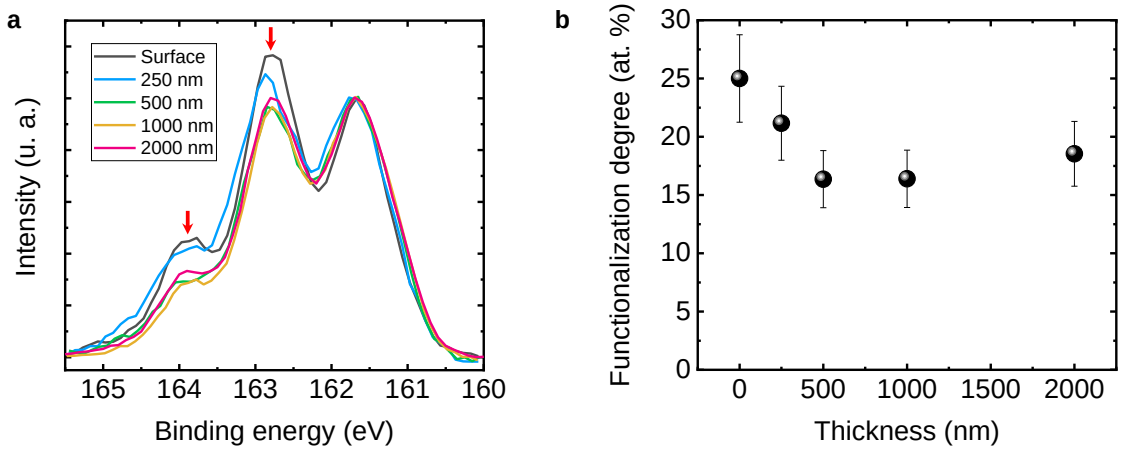

Supplementary Figure 27. a, Normalized high-resolution XPS spectra from the S2p region from MoS_2-Met. membranes with increasing thicknesses from 250 nm up to 2000 nm. **b**, Evolution of the functionalization degree per S atom of MoS_2-Met. membranes with thicknesses of 250 nm - 2000 nm. The functionalization degrees are estimated from the deconvolution of the S2p region.

shows the X-ray diffraction responses of membranes made of MoS_2 nanosheets functionalized with acetamide and methyl groups. We found that for both types of

membranes, the (002) peak is not significantly shifted; thus demonstrating that the interlayering spacing is largely preserved and independent of the membrane thickness. On the other hand, the full width at half maximum (FWHM) increases as the thickness increases from 250 nm up to 2000 nm suggesting that the degree of order of the vertical stacking of the MoS_2 nanosheets in the membranes reduces with the increase of the thickness of the membranes (a,b).

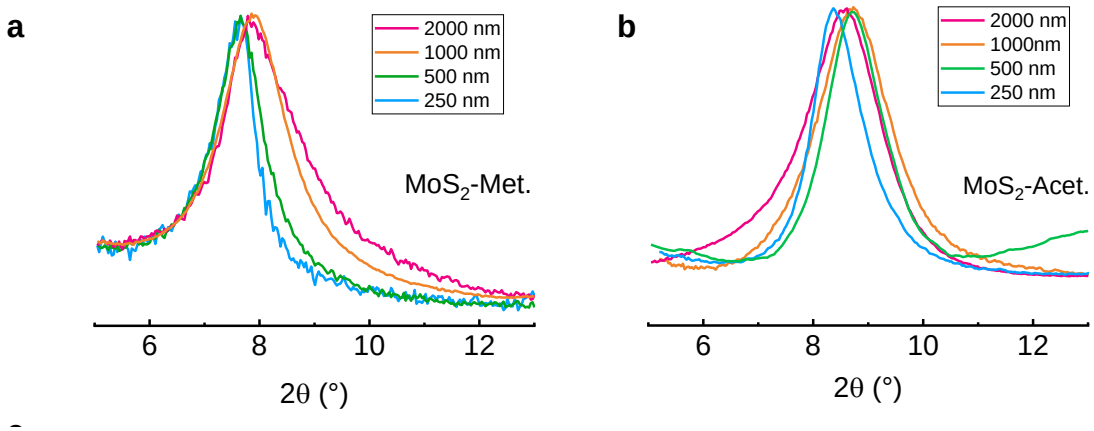

Supplementary Figure 28. Normalized X-ray diffraction spectra centered around of the (002) peak from the membranes made of methyl- (a) and acetamide- (b) functionalized MoS2 nanosheets with increasing thicknesses from 250 nm up to 2 000 nm.

We observed that the broadening of the (002) XRD peak for the MoS_2-Met. membranes deviates from the evolution of that of MoS_2-acet. membranes for thicknesses larger than 1000 nm suggesting further disorder in the case of methyl- functionalized MoS_2 nanosheets (a,b). We also analyzed the nanolaminate membranes made of ethyl-2-ol- functionalized MoS_2 nanosheets (prepared by the same method as for the MoS_2-Acet. membranes) and the same trend as for MoS_2-Acet. membranes was observed.

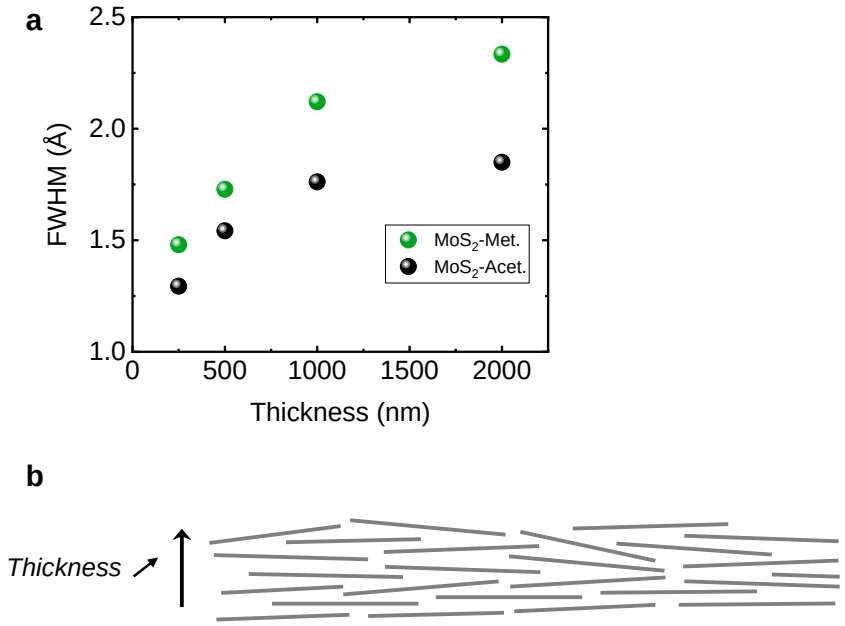

Supplementary Figure 29. a) Evolution of the full width at half maximum (FWHM) of the (002) peaks between 250 nm and 2000 nm. **b**) Schematic showing the influence of the vertical stacking of the nanosheets on the broadening of the (002) XRD peak of the functionalized MoS_2 membranes.

Interestingly the broadening of the (002) peak of MoS_2-Acet. membranes is symmetrical, while an asymmetry is clearly observed for the (002) peak of MoS_2-Met. (a,b). We attribute this phenomenon to a locally lower functionalization on the nanosheets likely due to a limited access of the reagents for the narrowest regions of the 2D capillaries. Indeed MoS_2-Met. membranes are functionalized on the support and the non-uniform interlayer spacing of the pristine MoS_2 membranes (,top) translates into non-uniform diffusion of the reagents such as iodomethane. This results in non-uniform functionalization (,bottom) as confirmed by the assymetric broadening of the (002) peak (a,b). On the other hand, the XPS analyses of the membranes revealed that the average functionalization degree of the membrane is constant (XPS measurements are averaged over a probed size of 400 µm in diameter). Therefore, because of *i)* the non-uniform

functionalization observed from the (002) peak and *ii)* the stable average functionalization degree of the membranes measured from the XPS analyses, we can conclude that for the regions of the membranes where the reagents can easily diffuse in, the extent of methyl groups is larger than the average value measured from the XPS analyses. At the opposite, for the other regions where the reagents have limited access due to steric hindrance, the extent of functional groups is smaller than the average ().

Since the functionalization degree remains constant even at larger thicknesses (Supplementary Figure 19b), we anticipate that as the thickness of the nanolaminate membranes increases, the non-uniform diffusion of the reagent increases and leads to more non-uniform grafting of the methyl groups. Our numerical simulations (See "Concentration of the functional groups" section for more details) have however predicted that the larger the amount of methyl on MoS_2, the larger the water flux. The unexpected water flux for thick MoS_2-Met. membranes is attributed to non-uniform functionalization degree and locally larger density of methyl groups on the nanosheets.

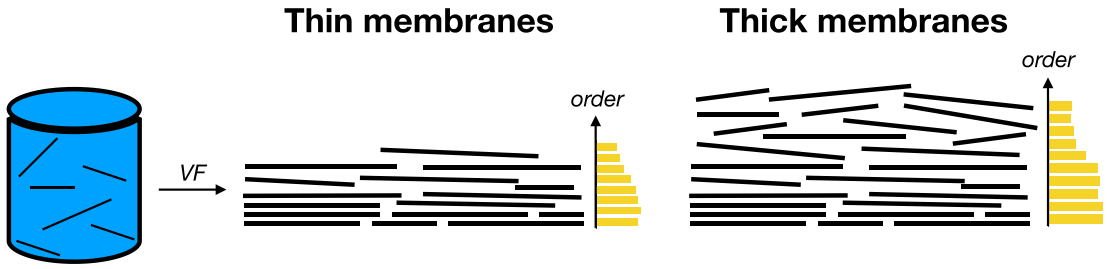

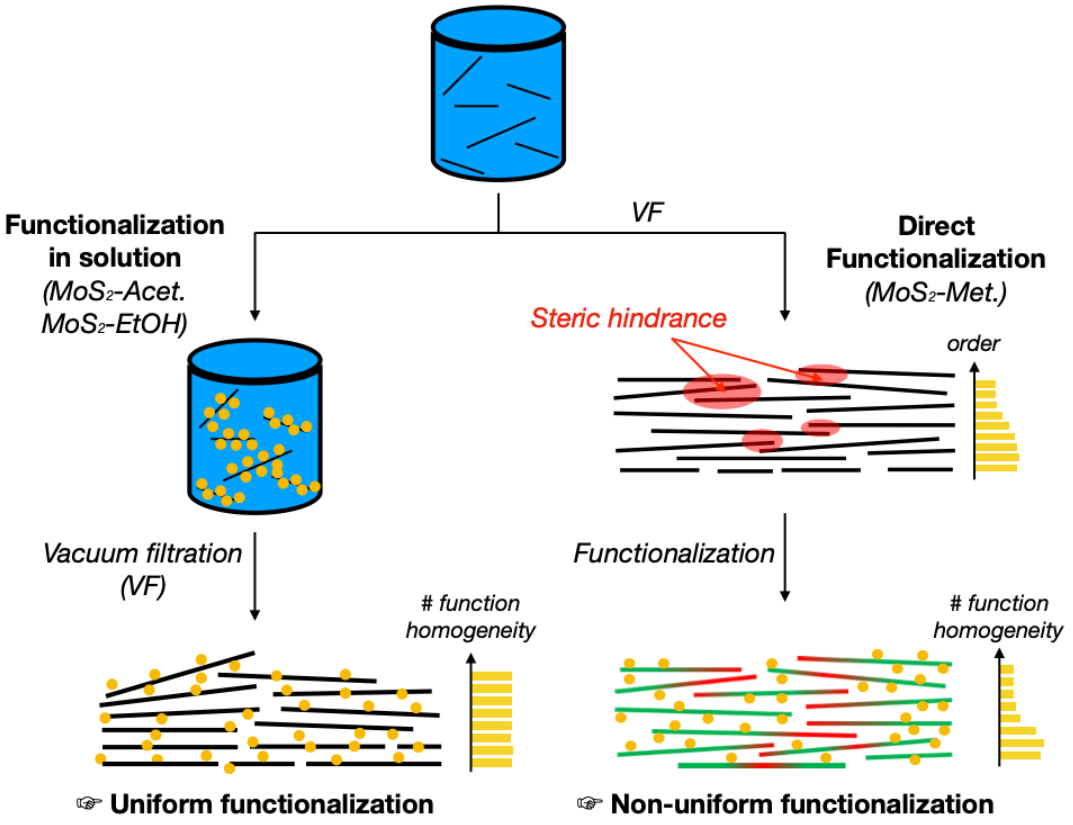

Supplementary Figure 30. Top: Representation of the turbostatic stacking of the nanosheets in the nanolaminate membranes prepared via vacuum filtration (VF). **Bottom:** Influence of the membrane fabrication on the functionalization homogeneity. In the case of MoS_2-Acet. and MoS_2-EtOH, the functionalization of the nanosheets is uniform because the nanosheets are functionalized in solution. In the case of the direct functionalization with iodomethane, the lower interlayer spacing limits the diffusion of the reagents due to steric hindrance. This translates into locally lower functionalization (in red) while the other regions are more decorated with methyl groups (in green).

Our results show that the nanosheets are slightly more functionalized on the top surface compared to the core of the membrane and the functionalization degree per S atom varies from 25% down to 19% for the top surface and the 2 µm-thick membrane respectively. Importantly our measurements also reveal that the amount of grafted

functional groups on the MoS_2 nanosheets in the membrane remains virtually constant for thicknesses as high as 2 μm. On the other hand, the full width at half maximum (FWHM) of the (002) XRD peak increases for all the membranes as the thickness increases. The FWHM of the (002) peak for the MoS_2-Met. membranes however deviates from the evolution of the (002) peak of MoS_2-Acet. membranes for thicknesses larger than 1 μm suggesting further disorder in the case of methyl-functionalized MoS_2 nanosheets (Supplementary Figs. 20,21).

Velocity profile and slip length measurements

We calculated the slip length for pristine MoS_2 and methyl-functionalized MoS_2. The slip length was obtained by fitting the velocity profile of water molecules inside wide 2D channels of approximately 40 Å separation following the method proposed by Wang et al.[21]. The velocity profiles and corresponding fits for pristine and methyl-MoS_2 are shown in Supplementary Figure 31. Our MD results show that the slip length L_S is –1.70 Å in the case of pristine MoS_2 nanosheets. A negative slip length is expected in the case of hydrophilic membranes. For example, negative slip length was predicted between charged graphene membranes and water in the aforementioned reference. The authors found that the values for L_S can be tuned from 78 Å for pristine graphene to -1.07 Å when partial charges are introduced. Since 1T' MoS_2 membranes are rather hydrophilic, our values of L_S are consistent with the results from Wang et al. In the case of methyl-functionalized MoS_2 membranes, L_S increases to -1.38 Å, consistent with the decrease of the hydrophilicity of the MoS_2 slabs. As discussed in the Molecular Dynamics section, the reactive force field overestimates surface tension at the MoS_2/water interface and

therefore leads to more hydrophilic MoS_2. However, this does not affect the comparative nature of the analysis between functional groups. Our simulations predict that the presence of methyl functional groups lead to improved slip length and velocity profiles due to less hydrophilic surface.

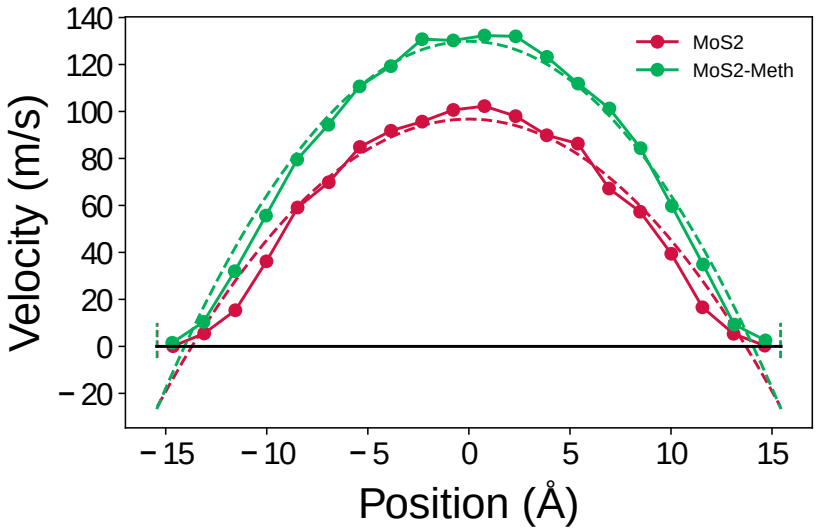

Supplementary Figure 31. Velocity profiles of water in pristine (red) and methyl-functionalized MoS_2 channels.

Molecular sieving performances under reversed osmosis conditions

To evaluate the sieving properties of membranes towards nanocontaminants, the MoS_2 membranes were tested under reverse osmosis (RO) conditions as described above. The upstream reservoir was filled with aqueous solution of caffeine, acetaminophen, estradiol β, or Ni-phtalocyanine (Nickel(II) phthalocyanine-tetrasulfonic acid tetrasodium salt, NiPc) (respectively with concentrations of 0.05 M, 0.5 M, 11 µM and 0.33 mM). Experiments have been performed at 2 bars loading for every contaminant solutions. The

permeate solutions were collected and analyzed using high performance liquid chromatography coupled UV-vis detector (HPLC/UV/Fluo). HPLC characterization has been recovered using an APEX WP ODS column (7µ 25cm/4.6 mm) and data analysis were performed with EMPOWER build 1154 software.

Physico-chemical properties of the contaminant tested are reported in Supplementary Table 7. The Stoke radius – that represents the effective hydrated size of molecules in water – has been calculated using *Equation (4).*

$$r = \frac{k_B \times T}{6\pi \times \eta \times D} \quad (4)$$

where k_B is Boltzmann's constant (1.38×10^{-23} J K^{-1}), T is the temperature (K), η the kinematic viscosity of the solvent (kg ms^{-1}) and D is the diffusion coefficient of the contaminants (m^2 s^{-1}).

Supplementary Table 7. Physico-chemical properties of contaminants. The Stoke radii were calculated at 25 °C. * Stoke radius of NiPc has been estimated based on the Stoke radius of porphyrin [22].

Contaminant	Structure	Molecular weight (g mol^{-1})	Stoke radius (nm)	Ref.
Caffeine	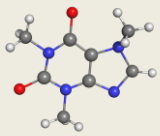	194.2	0.38	23

NiPc	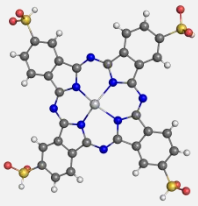	979.40	≈ 0.7-1	22
Acetaminophen (Paracetamol)	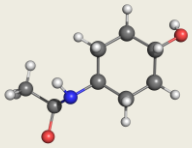	151.2	0.39	24
β-estradiol	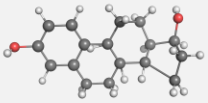	272.4	~0.5	25

Desalination performance under reverse osmosis conditions

The desalination performance was evaluated using the same methodology as for the nanocontaminants with a feed concentration of NaCl of 0.1 M (0.58 wt. %). The concentration of NaCl in the permeate was measured using Inductively Coupled Plasma Optical Emission Spectrometry (ICP-OES). ICP OES measurements were obtained using an ICAP 7400 ICP-OES Analyzer spectrometer (THERMO SCIENTIFIC). Supplementary Figure 32 summarizes the desalination performance of the various functionalized MoS_2 membranes under reverse osmosis configuration. Desalination peaks at 95 % NaCl rejection for methyl-functionalized membranes.

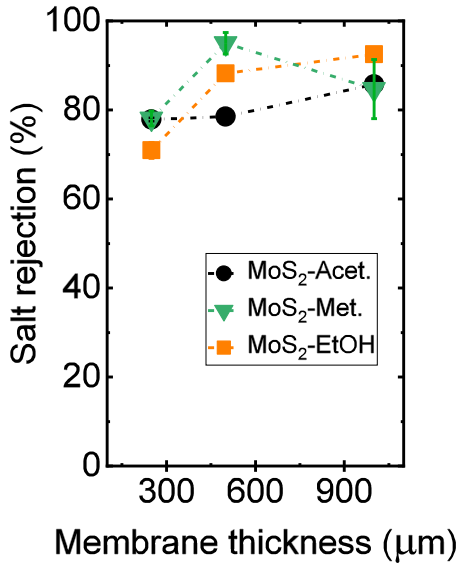

Supplementary Figure 32. NaCl rejection for the different functionalized MoS_2 membranes with thicknesses of 250 nm, 500 nm and 1 μm.

Under the same conditions (0.1 M NaCl), we tested the functionalized MoS_2 membranes towards desalination under reverse osmosis at an applied pressure of 9 bar. The rejection performances are largely maintained even at 9 bar (Supplementary Figure 33 Supplementary Figure 26 and Supplementary Table 8). We note that the values of water flux at 9 bar differ from those measured at lower pressures up to 4 bar due to differences in stiffness of the functionalized nanolaminate membranes.

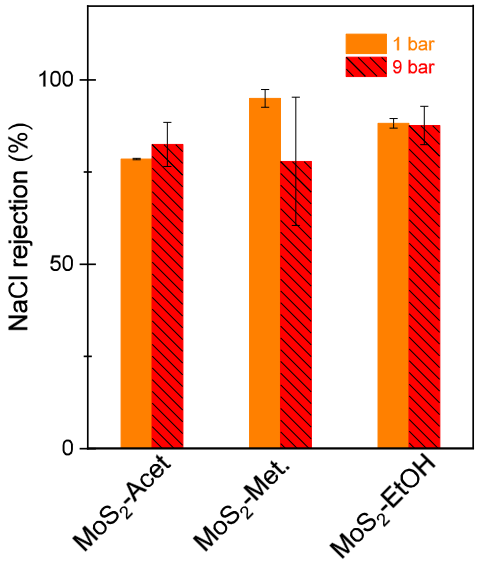

Supplementary Figure 33. Comparison of the desalination performance at 1 and 9 bar obtained for 500 nm-thick functionalized MoS_2 membrane.

Supplementary Table 8. Rejection performance of the 500 nm-thick functionalized MoS_2 membranes under a pressure of 9 bar.

Samples	NaCl Rejection at 1 bar (%)	NaCl Rejection at 9 bar (%)
MoS_2-Acet.	78.5 (± 0.2)	82.5 (± 6.0)
MoS_2-Met.	95.0 (± 2.4)	77.9 (± 17.4)
MoS_2-EtOH	88.2 (± 1.3)	87.6 (± 5.2)

Comparison of the performance of the MoS_2 membranes with the state of the arts

The desalination performances have been compared with the literature (main Figure 3D) and the corresponding data are detailed in **Supplementary Table 9**.

Supplementary Table 9. Comparison of the performances of functionalized MoS_2 membranes with performance from the state of the arts. RO: reverse osmosis; SWRO: Sea water Reverse Osmosis; BWRO: Brackish Water Reverse Osmosis; NF: Nanofiltration; NR: not reported; TFC: Thin Film Composite; CNT: Carbon Nanotube, GO: Graphene oxide.

Materials	Filtration method	Thickness (nm)	Press. (bar)	NaCl feed [] (M)	Water flux L/(h.m².bar)	NaCl rejection	Ref.
Non functionalized MoS_2	**Dead end**	**250-1000**	**0.5-4**	**0.1**	**0** ***(pure water)***	**-**	**This work**
Acetamide-functionalized MoS_2	**Dead end**	**250**	**1**	**0.1**	**13.7 (± 5.0)** ***(pure water)***	**77.9 (± 0.3)**	**This work**
		500			**9.3 (± 2.8)** ***(pure water)***	**78.5 (± 0.2)**	
		1000			**3.1 (± 1.6)** ***(pure water)***	**85.7 (± 0.2)**	
	FO	**1000**			**0.036 (± 0.006)**		
		250			**0.052 (± 0.005)**		
Acetamide-functionalized MoS_2	**Dead end**	**500**	**9**	**0.1**	**33.7 (± 13.5)**	**82.5 (± 6)**	**This work**
Ethyl-2-ol-functionalized MoS_2	**Dead end**	**250**	**1**	**0.1**	**42.5 (± 12.1)** ***(pure water)***	**70.9(± 1.8)**	**This work**
		500			**13.4 (± 3.0)** ***(pure water)***	**88.2 (± 1.2)**	
		1000			**7.8 (± 5.0)** ***(pure water)***	**85.7 (± 1.0)**	
		2000			**2.1 (± 0.4)** ***(pure water)***		

	FO	**1000** **250**			**0.092 (± 0.02)** **0.146 (± 0.04)**		
Ethyl-2-ol-functionalized MoS_2	**Dead end**	**500**	**9**	**0.1**	**1.6 (± 0.53)**	**87.6 (± 5.2)**	**This work**
Methyl-functionalized MoS_2	**Dead end**	**250** **500** **1000** **2000**	**1**	**0.1**	**2.9 (± 1.6)** ***(pure water)*** **15.9 (± 4.0)** ***(pure water)*** **9.8 (± 5.2)** ***(pure water)*** **24.8 (± 0.6)** ***(pure water)***	**78.1(± 1.6)** **95.0 (± 2.4)** **84.7 (± 6.6)**	**This work**
Methyl-functionalized MoS_2	**Dead end**	**500**	**9**	**0.1**	**6.7 (± 1.35)**	**77.9 (±17.4)**	**This work**
Higly laminated GO	Dead end	8	2	1	4	25	26
Higly laminated GO	Dead end	150	2		0.3		26
MoS_2	Dead end	1700	1		245	NR	27
GO/TMC	Dead end	14	3.4	0.02	≈50	19	28
Graphene	Dead end	260-330	1	0.02	20	40	14
GO/CNT	Dead end	<100	5	0.01	5.5	59	29
Graphene/CNT	Dead end	≈40	5	0.01	11.3	51	29
GO/ PECs	Cross flow	-	5	-	0.7992	43	30
Graphene/CNT	Cross flow	-	5	0.01	12.13	39.6	29
Graphene/GO	Cross flow	260-330	50	0.04	0.34 (± 0.1)	85 (± 2)	31

Graphene/GO	Cross flow	260-330	50	0.04	0.22 (± 0.1)	54 (± 5)	31
Graphene/GO	Cross flow	260-330	50	0.04	0.46 (± 0.2)	85 (± 1)	31
Graphene/GO	Cross flow	260-330	50	0.04	0.38 (± 0.1)	85 (± 7)	31
Graphene/GO	Cross flow	260-330	50	0.04 0.55	0.44 (± 0.02) NR	83 (± 5) 35 (± 10)	31
Graphene/GO	Cross flow	260-330	50	0.04	0.67 (± 0.2)	79 (± 8)	31
Graphene/GO	Cross flow	260-330	50	0.04	6.72 (± 3.8)	26 (± 8)	31
Graphene/GO	Cross flow	260-330	40	0.04	0.36 (± 1.1)	83 (± 3)	31
Graphene/GO	Cross flow	260-330	40	0.04	0.15 (± 0.07)	80 (± 5)	31
Graphene/GO	Cross flow	260-330	40	0.04	0.43 (± 0.2)	81 (± 2)	31
Graphene/GO	Cross flow	260-330	40	0.04	0.34 (±± 0.2)	82 (±± 8)	31
Graphene/GO	Cross flow	260-330	40	0.04	0.40 (± 0.01)	82 (± 4)	31
Graphene/GO	Cross flow	260-330	40	0.04	0.64 (± 0.2)	77 (± 9)	31
Graphene/GO	Cross flow	260-330	40	0.04	6.50 (± 3.7)	25 (± 8)	31
Porous graphene	Cross flow	-	0.25	-	2.5	-	10
Zeolite	Cross flow	3000	20.7	0.1	0.005	76.7	27
CNT	Pressure retarded osmosis	-	-	_	36 (± 54)	60 (± 10)	28
Commercial TFC	Cross flow	tubular	55.2	0.0006	0.015	99.75	32
Commercial desalination membrane (2011) SWRO	Cross flow	tubular	55.1	≈0.5	0.3 (± 0.1)	99.5 (± 0.5)	32

BWRO	Cross flow	tubular	6.9-41.4	0.0086 - 0.034	2 (± 2)	94 (± 1.425)	32
NF	Cross flow	tubular	5.2-15.9	0.0086 - 0.034	5.5 (± 1)	65 (± 15)	32
Commercial TFC (2016)	Cross flow	Spiral wound	55	≈0.5	1.19 (± 0.24)	99.7	33
Commercial TFC (US, 2017)	Cross flow	Spiral wound	56	≈0.5	0.68 (± 0.14)	99.8	34
Commercial TFC polyamide	Cross flow	spiral wound	15.5	≈0.55	2.8	99.5	35
Commercial TFC polyamide	Cross flow	spiral wound	55	≈0.55	0.47	99.7	36
Commercial TFC polyamide	Cross flow	spiral wound	55	≈0.55	0.85	99.7	37
Commercial TFC polyamide	Cross flow	spiral wound	55	≈0.55	0.7	99.5	38
Commercial TFC polyamide	Cross flow	spiral wound	55	≈0.55	0.57	99.7	39
Commercial TFC polyamide	Cross flow	spiral wound	55	≈0.55	0,49	99.7	40
Commercial TFC polyamide	Cross flow	spiral wound	55	≈0.55	0,62	99.7	41
Commercial TFC polyamide	Cross flow	spiral wound	55	≈0.55	0,63	99.7	42

Graphene	Dead-end	53	5	0.02	3,26	≈42	14
GO	FO	0.28	0.28		0.068 (± 0.007	90	18
GO	FO	0.28	0.28		0.029 (± 0.005)	90	18
GO/graphene	FO	0.1	5		0.0034	NR	10
GO/graphene	FO	1	1		0.035	≈ 94	10
GO/graphene	FO	0.1	5		0.007	97	10
GO	FO	5	5		0.0084	60	10
GO	FO	1	1		0.008	NR	11
MoS_2	FO	1	1		0.0022	NR	17
Dye decorated MoS_2	FO	3 5 6		0.1	0.04 0.033 0.0116	NR 99 NR	5
Dye decorated MoS_2	Dead end	5	1	1	270	≈ 20 %	5
2D/0D GO	Dead end		1.5	0.02	128.45	≈ 15 %	43
GO	Dead end		1.5	0.02	16.94	50.1	43

Molecular dynamics simulations

Reactive MD and interatomic potential

We performed fully reactive molecular dynamics simulations with ReaxFF [45]. C, H, O and N force field parameters were taken from Ref. [45] and combined with that of MoS_2 from Ref. [46]. We slightly modified the S-O van der Waals (vdW) parameters to improve the water/MoS_2 interactions. These parameters have been optimized against density functional theory (DFT) calculations corresponding to the adsorption of a single water molecule on a monolayer MoS_2 and, water molecules in between MoS_2 layers. Supplementary Figure 34 shows the corresponding potential energy surfaces before and after optimization of the parameters, summarized in Supplementary Table 10. We note that this adjustment only affects the water/MoS_2 interactions since sulfur is not part of any functional group studied. Second order interactions such as Mo with C, H, O and N were taken from Ref.[47].

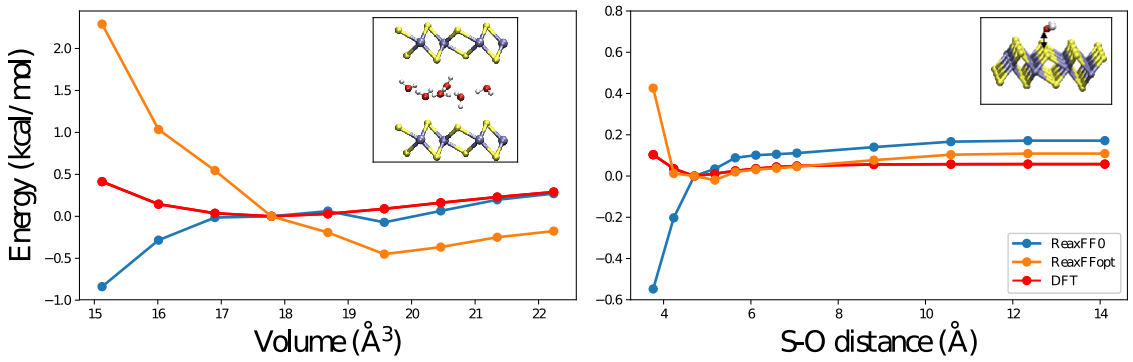

Supplementary Figure 34. ReaxFF optimization. ReaxFF was optimized to describe the energy of bulk MoS_2 intercalated with 6 water molecules as a function of the out of plane lattice parameter (left) and, the adsorption of a water molecule on the surface of MoS_2 as a function of S-O distance (right).

Supplementary Table 10. Original and optimized ReaxFF off-diagonal parameters for S-O interaction.

	Ediss	Ro	Gamma	rsigma
Original from Ref. 45	0.1962	1.7872	10.2319	1.4622
Optimized parameters	0.2132	2.2373	11.3611	1.1245

We acknowledge that our reactive force field does not lead to stable water drop on a perfect MoS_2 surface, as it is often used to validate the water/surface interaction[48]. Although there is no proof that the adhesion of a water drop on surface and its confinement in sub-nanometer channels behave similarly[49]. We found that the water drop completely wet the MoS_2 surface after approximately 1 ns of equilibration. Therefore, our model overestimates surface tension at the water/MoS_2 interface and as a consequence, underestimates the absolute water flux. However, the relative flux between different MoS_2 functionalized surfaces and various interlayer spacing discussed here are relevant. Moreover, we want to stress that the proposed reactive force field is the only model available to describe with precision such complex surfaces including partial charges and polarization effects including that of the lone pairs on O and S elements. Preliminary tests with state-of-the-art water/MoS_2 interatomic potentials led to very high hydrophobicity of the functionalized channels mainly because of the static description of partial charges and the lack of parameters for inorganic/organic surfaces[50]. Future work should focus on the improvement of the reactive force field in order to improve the description of the contact angle of water on MoS_2 surface.

DFT calculations were performed with VASP[51,52] with the Perdew, Burke, and Ernzerhof functional[53] including Grimme's D2 correction to improve vdW interactions[54]. Both monolayer and bulk supercells were built by replicating 4×4 times the rectangular unit cell of MoS_2 in the in-plane directions. A 2×2×1 and 1×1×2 k-grid was used for monolayer and bulk calculations, respectively. We used a 400 eV kinetic energy cutoff and, we assumed convergence when energy and forces reached thresholds of 10^{-4} eV and 5×10^{-2} eV $Å^{-1}$, respectively.

Nanofluidic simulations

Nanofluidic transport simulations were performed using the fluctuating wall method. We followed ideas from Berendsen's thermostat[55] to adjust the position of two harmonic walls (which interact with water via a simple harmonic potential) perpendicular to the channel and located at the boundaries of the simulation cell (main Figure 4a). The position of one wall *x* at time *t* is defined as in Equation *(5):*

$$\begin{cases} \mu = 1 - \beta \frac{\Delta t}{\tau}(P - P_{ext}) \\ x = x_0 + \mu v_0 t \end{cases} \quad (5)$$

with x_0, v_0 the initial position and velocity of the wall, μ a scaling factor computed every 10 steps in the present simulations, β the compressibility, Δt the time step, τ a time constant, P_{ext} the target pressure and P the pressure computed as the total force on the wall divided by its area. β and τ were optimized to reach fast pressure equilibration resulting in the values 0.05 and 10000, respectively. The external pressure on the feed

and permeate walls is represented on Supplementary Figure 35. A 500 MPa pressure gradient is achieved by setting the pressure of the feed reservoir to 510 MPa and that of the permeate reservoir to 10 MPa. The water flux was computed from the slope of the number of water molecules crossing the mid-point of the nanochannel as a function of simulation time. We converted units from the number of water molecules per nanoseconds (water ns^{-1}) to L m^{-2} h^{-1} bar^{-1} by normalizing with the area of the channel (lenght×width) and dividing by the applied pressure of 500 MPa. The number of water molecule per liter was calculated assuming a water density of 1 g cm^{-3}.

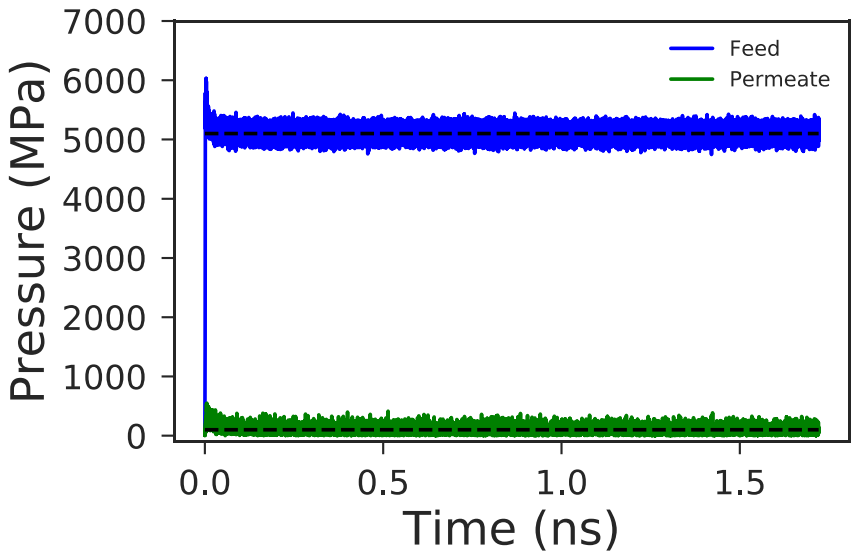

Supplementary Figure 35. Applied pressure on the feed and permeate reservoir using the fluctuating wall method as a function of simulations time. The target pressures are 510 and 10 MPa applied to the feed and permeate reservoirs, respectively.

.

Density Profiles

We performed density profiles of O and H atoms along the y-direction (see main Figure 4a for the reference frame axis) to characterize the structure of water in various nanochannels. Supplementary Figure 36 shows density profiles of pristine MoS_2 nanochannels at different capillary widths (corresponding to simulations presented Figure 4b in the main text). For pristine MoS_2 channels, we found that water molecules are highly organized in layered structure.

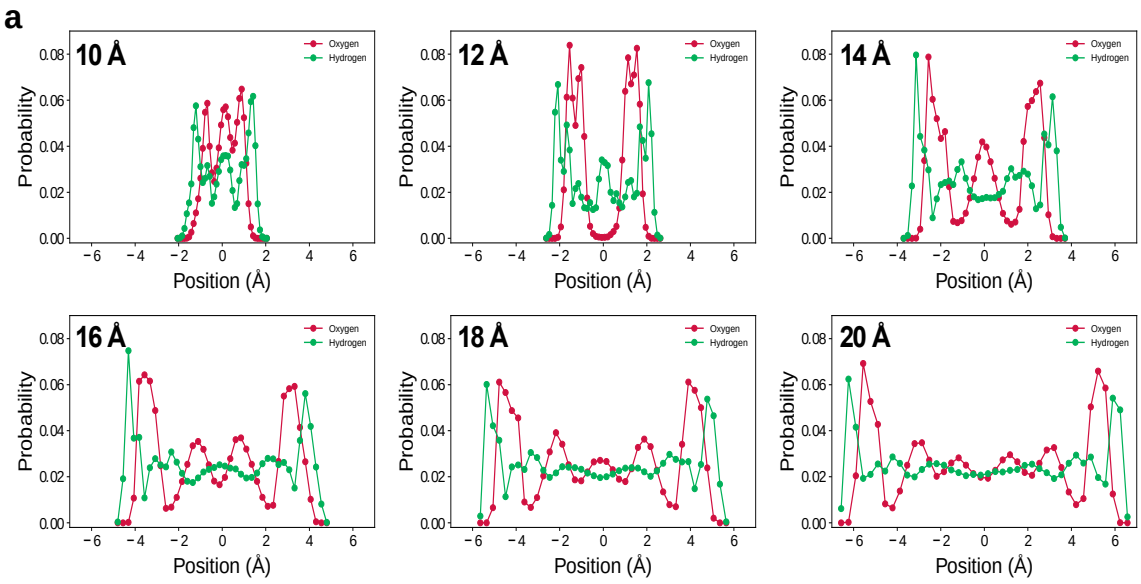

Supplementary Figure 36. Density profiles of O and H along the y-direction for pristine MoS_2 channels at various capillary widths.

We identified 1, 2, 3, 4, 5 and 6 layers of water in capillaries width of 10, 12, 14, 16, 18 and 20 Å, respectively. This agrees well with recent equilibrium MD simulations [56] for which the structure of water was associated with the electrostatic interactions between water and MoS_2. The introduction of methyl-functionalized channels leads to the

enlargement of the oxygen peaks at 12 Å separation and, the loss of the 6-layers structure at 20 Å capillary width, compared to pristine channels (Supplementary Figure 37b,d). This shows that water between methyl functionalized channels is less structured compared to water between pristine walls.

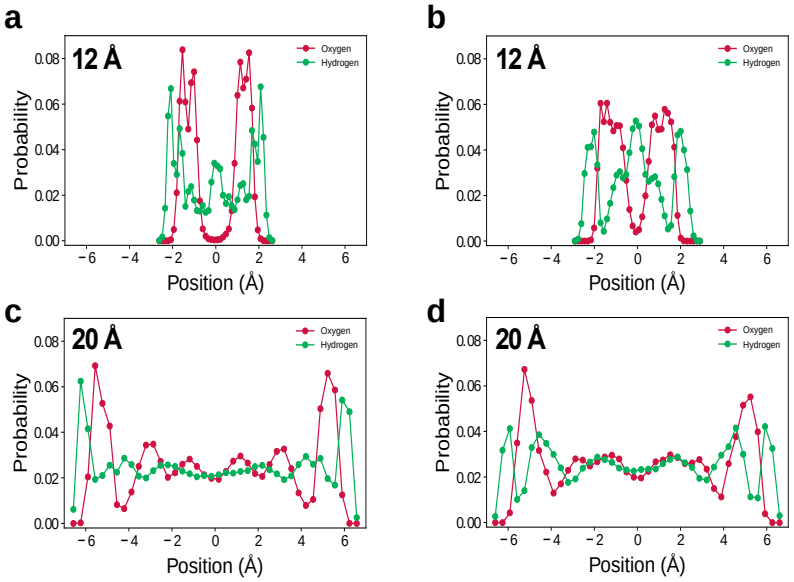

Supplementary Figure 37. Density profiles of O and H along the y-direction for pristine (**a,c**) and methyl-functionalized (**b,d**) MoS_2 channels at various capillary widths.

Axial density function

The structure of water along the flux direction (x-axis) can be characterized by the axial density function (ADF)[49]. Similar to the radial pair distribution function, the ADF a(x) represents the probability of finding a water molecule within the interval x and x+dx from a reference water molecule. The ADF is normalized such that its integral over the entire channel equals the total number of water molecules. The ADF for pristine, methyl, acetamide and ethyl-2-ol functionalized channels (corresponding to data in main Figure

4f) are represented Supplementary Figure 38. Because of the non-periodicity of the channel in the X-direction, the probability of finding a water molecule decreases when x increases. For pristine case, we can clearly identify the structure of water in the axial direction with a period of approximately 3 Å. No clear structure is observed for the functionalized cases.

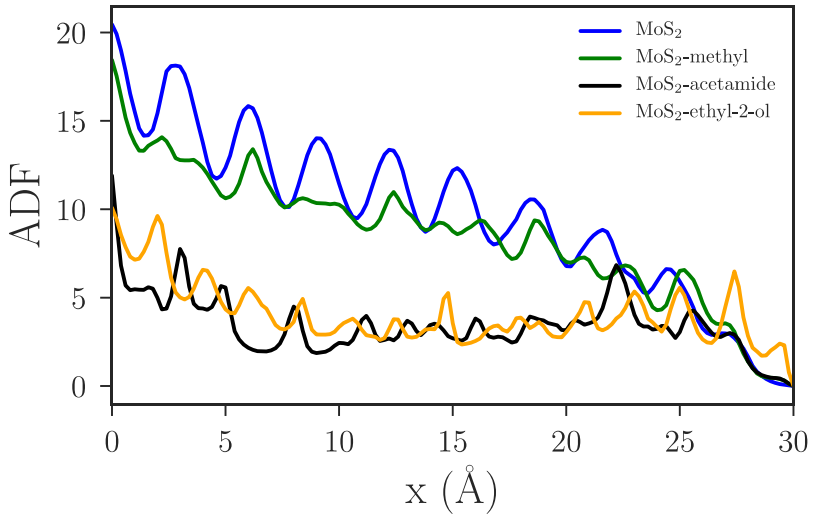

Supplementary Figure 38. Axial density function along the channel direction for various functionalized channels separated by 12 Å.

Hydrogen bond correlation function.

The dynamical properties of water confined can be determined from the hydrogen bond correlation function Hbcorr(t) [57]. We define a hydrogen bond between two water molecules when the distance between their oxygen atoms is less than 3.5 Å and the angle between the vector joining the two oxygen atoms and that corresponding to the O-D bond of the donor water molecule is less than 30° [57]. The hydrogen bond correlation function is then calculated as Hbcorr(t) = <h(0)h(t)>/h with h(t) = 1 when a hydrogen bond exists

for a particular tagged pair of water molecules and zero otherwise. The hydrogen bond correlation function corresponds to the probability that there is a hydrogen bond at time t, given that it was already established at time zero. We show in Supplementary Figure 39 the hydrogen bond correlation function of bulk water and water between various functionalized MoS_2 channels, separated by 12 Å (corresponding to data in main Figure 4f). The hydrogen bond lifetime is evaluated from the fit of the curves with the exponential e-t/τ and, are reported in the legend of the figure. We found lifetimes of approximately 1 ns for water inside 12 Å MoS_2 capillaries, two orders of magnitude higher than in bulk water. This demonstrates that the interactions between water molecules in confined MoS_2 channels are much stronger than in the bulk, characteristic of an ice-like structure and, similar to the arrangement of the water molecules inside carbon nanotubes. The presence of non-polar functional group such as methyl lowers lifetimes by approximately a factor of 2 leading to more bulk-like water.

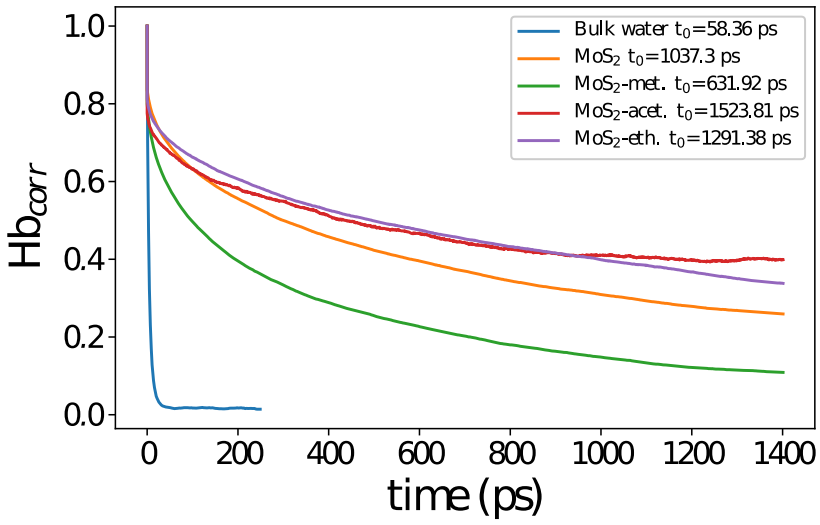

Supplementary Figure 39. Hydrogen bond correlation function of bulk water and water between various functionalized MoS_2 channels separated by 12 Å.

Velocity map.

We found that confined water in MoS_2 channels is highly organized with slow hydrogen bond relaxation timescales forming ice-like layers. We now investigate the correlation between the structure of the nanochannel and the dynamical properties of water. More precisely, we would like to see if there is any correlation between the mobility of water in contact with the pristine or functionalized surfaces. We computed the velocity of the first layer of water molecules in contact with pristine and methyl-functionalized MoS_2. Supplementary Figure 40 shows the representations of the methyl-MoS_2 channel side by side including the time averaged velocity map of water (as in main Figure 4e), the same map with in addition all positions of C and H atoms of methyl functional groups during the time averaged, and the actual molecular model of the layer of the channel showing all positions of the methyl atoms during the time average. By comparing the 3-graphs, one can conclude that the large majority of methyl atoms' location corresponds to higher averaged velocity of the water molecules underneath. Red (high velocity of water) patches are completely covered by the positions of methyl's atoms.

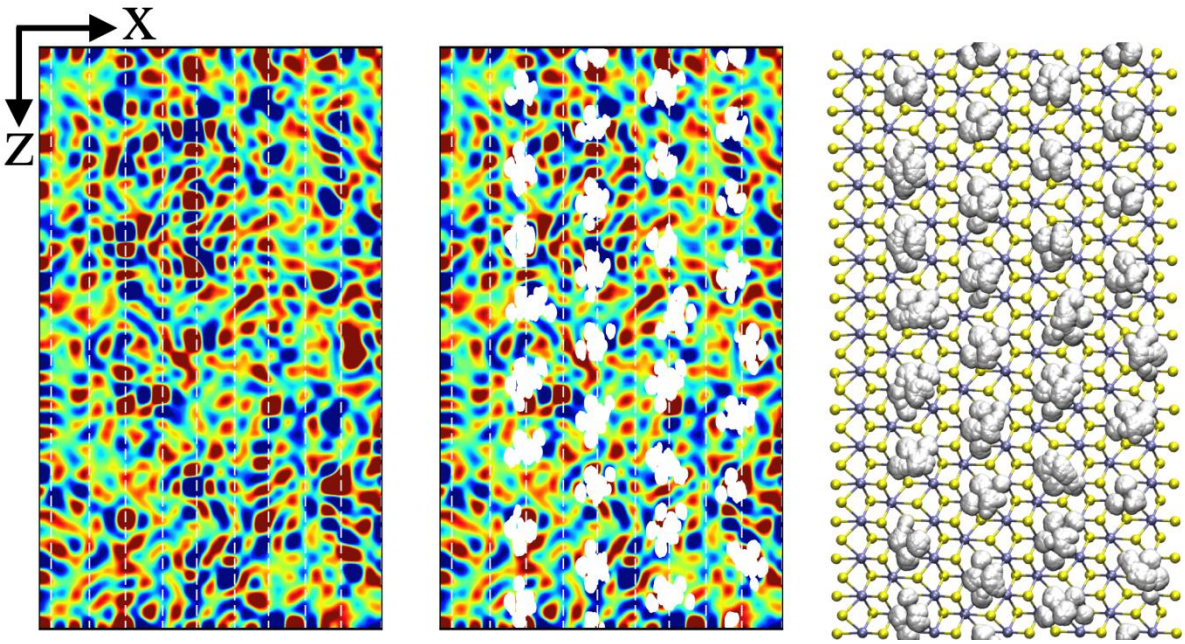

Supplementary Figure 40. From left to right, time averaged velocity map of the first layer of water molecules in the XZ plane of methyl-functionalized MoS_2 membranes, same map including the actual position of the C and H atoms of the methyl group during the time averaged simulation, and molecular model of the layer of methyl-MoS_2 channel. Vertical white dashed lines correspond to the location of S atoms along the flux direction..

Indeed, we can see from main Figure 4c that the top and bottom S-atoms of the channel are slightly shifted in x. The velocity of each water molecule of the selected layer are averaged into 1 $Å^2$ bins along the 1 ns trajectory and interpolated for better clarity. The velocity maps and their projection along the x-axis are represented in Supplementary Figure 41 together with the position of the nearest S-atoms of the MoS_2 layer as white (map) and black (projection) dashed lines. Because of the limited amount of data (1 ns), the averaged velocities are quite large however, we can clearly see from the maps the higher mobility of water molecules in contact with methyl-functionalized MoS_2. We note that minima in the velocity projection along the pristine channel are aligned with the

location of S-atoms. By contrast, maxima in the velocity projection along methyl-functionalized channel are aligned with S-atoms. From this, we conclude that S atoms represent "pinning points" between highly polarized Mo-S and O-H bonds of electrostatic nature. The presence of methyl groups substitutes some of these pinning points and enhances the velocity of water molecules located below them. These results thus predict that the hydrophobic nature of methyl functionalized membranes is responsible for the enhanced water flux.

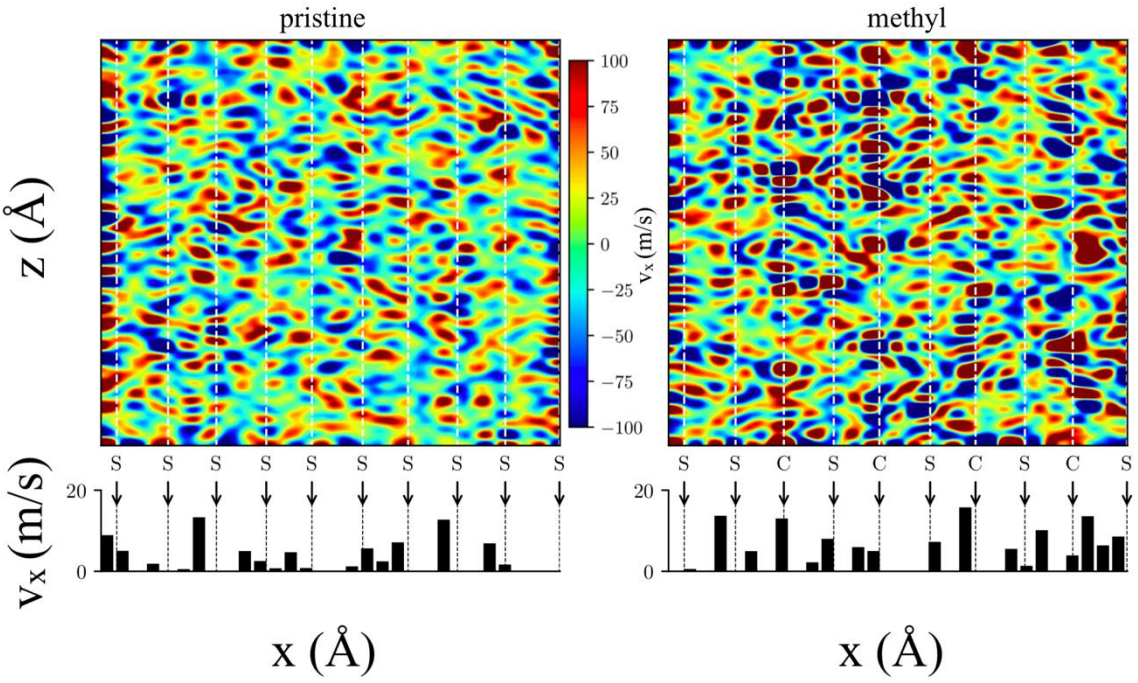

Supplementary Figure 41. Time averaged velocity map of the first layer of water molecules in the XZ plane and its projection along the channel direction. The velocity of water molecules is enhanced by the presence of methyl groups.

Size effect of functional groups

Since the ADF is normalized to the average number of water molecules in the channel, we can see from the area under the curve that much less water molecules are present

between acetamide and ethyl-2-ol functionalized channels. This can be attributed to steric effects of the large functional groups. Integrating the curves gives 292, 256, 104 and 123 water molecules for pristine (non-functionalized), methyl, acetamide and ethyl-2-ol functionalized MoS_2 channels. Additionally, we show Supplementary Figure 42 the position of oxygen and hydrogen atoms from water in the channels as red and gray dots, respectively, accumulated over 1,000 MD frames (=500 ps) of the simulations presented Figure 4f. We can see that water molecules in pristine and methyl-functionalized MoS_2 explored most of the volume available in the nanochannel. By contrast, water in acetamide and ethyl-2-ol functionalized MoS_2 are segregated in various regions of the channel. This confirms the steric effect of large functional groups and their limitation to water flow.

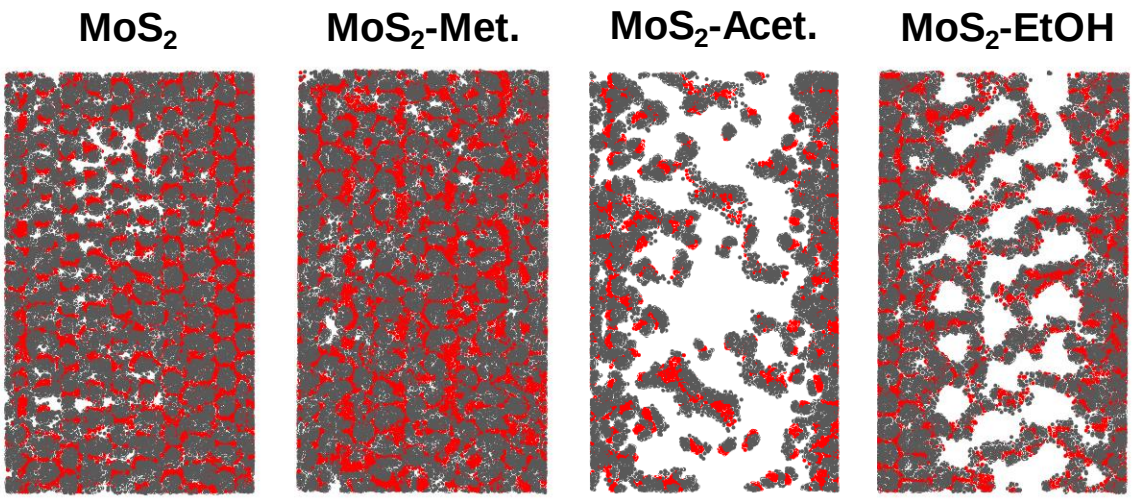

Supplementary Figure 42. Position of oxygen (red) and hydrogen (gray) atoms in pristine, methyl, acetamide and ethyl-2-ol channels accumulated during 500 ps of nanofluidic simulation.

Concentration of the functional groups.

Since S-atoms represent pinning points for water and that the methyl-functionalization is assumed to enhance water mobility, the flux should be directly proportional to the fraction of functionalized S-atoms. We performed nanofluidic simulations, similar to those presented section "Nanofluidic simulations", for 12, 25 and 50 % methyl-functionalized MoS_2 channels. Supplementary Figure 43 shows the corresponding number of water molecules crossing the channel as a function of simulation time. We found fluxes of 6.2, 15.7 and 31.1 $L.h^{-1}.m^{-2}.bar^{-1}$ for 12, 25 and 50 % methyl-functionalized MoS_2 channels, respectively. The near-perfect correlation between fluxes and the fraction of functionalized S-atoms demonstrates the surface mechanism of functional group to enhance water flow.

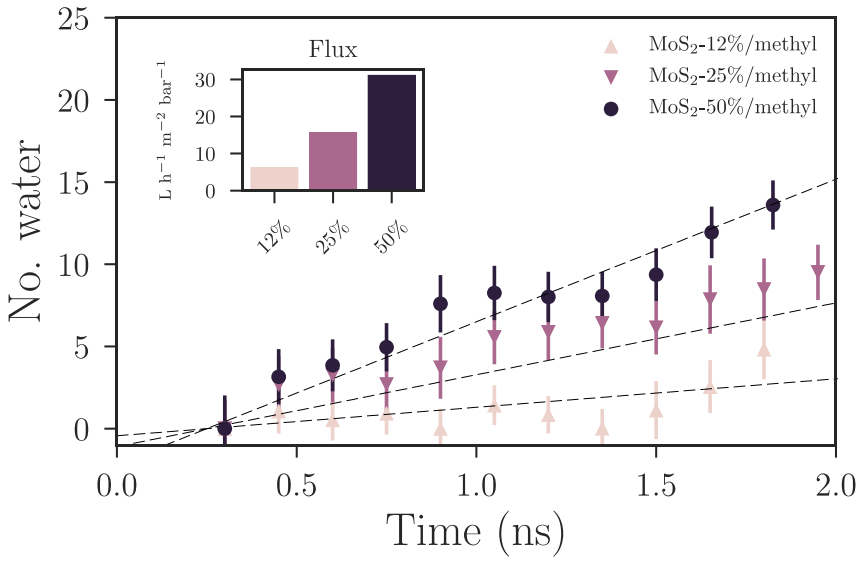

Supplementary Figure 43. Number of water molecules crossing the mid-point of the nanochannel as a function of simulation time for 12, 25 and 50 % methyl-functionalized MoS_2. The corresponding water fluxes are summarized in the inset.

References

1. Heising, J. & Kanatzidis, M. G. Structure of Restacked MoS_2 and WS_2 Elucidated by Electron Crystallography. *J. Am. Chem. Soc.* **121**, 638–643 (1999).
2. Voiry, D. *et al.* The role of electronic coupling between substrate and 2D MoS2 nanosheets in electrocatalytic production of hydrogen. *Nat. Mater.* **15**, 1003–1009 (2016).
3. Chow, P. K. *et al.* Wetting of Mono and Few-Layered WS_2 and MoS_2 Films Supported on Si/SiO_2 Substrates. *ACS Nano* **9**, 3023–3031 (2015).
4. Heising, J. & Kanatzidis, M. G. Exfoliated and Restacked MoS_2 and WS_2 : Ionic or Neutral Species? Encapsulation and Ordering of Hard Electropositive Cations. *J. Am. Chem. Soc.* **121**, 11720–11732 (1999).
5. Hirunpinyopas, W. *et al.* Desalination and Nanofiltration through Functionalized Laminar MoS_2 Membranes. *ACS Nano* **11**, 11082–11090 (2017).
6. Hirata, M., Gotou, T., Horiuchi, S., Fujiwara, M. & Ohba, M. Thin-film particles of graphite oxide 1: *Carbon* **42**, 2929–2937 (2004).
7. Voiry, D. *et al.* Covalent functionalization of monolayered transition metal dichalcogenides by phase engineering. *Nat. Chem.* **7**, 45–49 (2015).
8. Shen, Y., Wang, H., Zhang, X. & Zhang, Y. MoS_2 Nanosheets Functionalized Composite Mixed Matrix Membrane for Enhanced CO_2 Capture via Surface Drop-Coating Method. *ACS Appl. Mater. Interfaces* **8**, 23371–23378 (2016).
9. Calandra, M. Chemically exfoliated single-layer MoS 2 : Stability, lattice dynamics, and catalytic adsorption from first principles. *Phys. Rev. B* **88**, (2013).

10. Abraham, J. *et al.* Tunable sieving of ions using graphene oxide membranes. *Nat. Nanotechnol.* **12**, 546–550 (2017).
11. Joshi, R. K. *et al.* Precise and Ultrafast Molecular Sieving Through Graphene Oxide Membranes. *Science* **343**, 752–754 (2014).
12. Varrla, E. *et al.* Large-Scale Production of Size-Controlled MoS_2 Nanosheets by Shear Exfoliation. *Chem. Mater.* **27**, 1129–1139 (2015).
13. Neese, F. The ORCA program system: The ORCA program system. *Wiley Interdiscip. Rev. Comput. Mol. Sci.* **2**, 73–78 (2012).
14. Han, Y., Xu, Z. & Gao, C. Ultrathin graphene nanofiltration membrane for water purification. *Adv. Funct. Mater.* **23**, 3693–3700 (2013).
15. Derek W. Smith. Ionic hydration enthalpies.pdf. (1977).
16. Picaud, F. *et al.* Biomimetic solution against dewetting in a highly hydrophobic nanopore. *Soft Matter* **12**, 4903–4911 (2016).
17. Deng, M., Kwac, K., Li, M., Jung, Y. & Park, H. G. Stability, Molecular Sieving, and Ion Diffusion Selectivity of a Lamellar Membrane from Two-Dimensional Molybdenum Disulfide. *Nano Lett.* **17**, 2342–2348 (2017).
18. Chen, L. *et al.* Ion sieving in graphene oxide membranes via cationic control of interlayer spacing. *Nature* **550**, 380 (2017).
19. Suk, M. E. & Aluru, N. R. Water Transport through Ultrathin Graphene. *J. Phys. Chem. Lett.* **1**, 1590–1594 (2010).
20. Chong, J. Y., Wang, B., Mattevi, C. & Li, K. Dynamic microstructure of graphene oxide membranes and the permeation flux. *J. Membr. Sci.* **549**, 385–392 (2018).

21. Xu, F., Song, Y., Wei, M. & Wang, Y. Water Flow through Interlayer Channels of Two-Dimensional Materials with Various Hydrophilicities. *J. Phys. Chem. C* **122**, 15772–15779 (2018).
22. Kang, B. *et al.* Catalytically active supramolecular porphyrin boxes: acceleration of the methanolysis of phosphate triesters via a combination of increased local nucleophilicity and reactant encapsulation. *Chem. Sci.* **3**, 1938 (2012).
23. Price, W. E. Tracer caffeine diffusion in aqueous solutions at 298 K. The effect of caffeine self-association. *J. Chem. Soc. Faraday Trans. 1 Phys. Chem. Condens. Phases* **85**, 415–419 (1989).
24. Ribeiro, A. C. F. *et al.* Diffusion coefficients of paracetamol in aqueous solutions. *J. Chem. Thermodyn.* **54**, 97–99 (2012).
25. Drug Design: Medicinal Chemistry: A Series of Monographs, Volume 4.
26. Yang, Q. *et al.* Ultrathin graphene-based membrane with precise molecular sieving and ultrafast solvent permeation. *Nat. Mater.* **16**, 1198 (2017).
27. Sun, L., Huang, H. & Peng, X. Laminar MoS2 membranes for molecule separation. *Chem. Commun.* **49**, 10718 (2013).
28. Hu, M. & Mi, B. Enabling Graphene Oxide Nanosheets as Water Separation Membranes. *Environ. Sci. Technol.* **47**, 3715–3723 (2013).
29. Han, Y., Jiang, Y. & Gao, C. High-Flux Graphene Oxide Nanofiltration Membrane Intercalated by Carbon Nanotubes. *ACS Appl. Mater. Interfaces* **7**, 8147–8155 (2015).

30. Wang, N., Ji, S., Zhang, G., Li, J. & Wang, L. Self-assembly of graphene oxide and polyelectrolyte complex nanohybrid membranes for nanofiltration and pervaporation. *Chem. Eng. J.* **213**, 318–329 (2012).
31. Morelos-Gomez, A. *et al.* Effective NaCl and dye rejection of hybrid graphene oxide/graphene layered membranes. *Nat. Nanotechnol.* **12**, 1083–1088 (2017).
32. Geise, G. M., Park, H. B., Sagle, A. C., Freeman, B. D. & McGrath, J. E. Water permeability and water/salt selectivity tradeoff in polymers for desalination. *J. Membr. Sci.* **369**, 130–138 (2011).
33. Veolia, B. W. E., MBROYN307130. RO MEMBRANES VRO-SE4040. (2016).
34. Veolia, S. W. E. M. RO MEMBRANES VRO-400-28. (2016).
35. Brackish Water element BW30-440i High Surface Area - Dow FILMTEC™ Membranes - Form No. 609-00204-1108.
36. Sea Water element SW30XHR-400i- Dow FILMTEC™ Membranes - Form No. 609-00204-1108.
37. Sea Water element SW30ULE-400i - Dow FILMTEC™ Membranes - Form No. 609-00204-1108.
38. Sea Water element SW30XLE-400i - Dow FILMTEC™ Membranes - Form No. 609-00204-1108.
39. Sea Water element SW30HR LE-400i - Dow FILMTEC™ Membranes - Form No. 609-00204-1108.
40. Sea Water element SW30HR LE-400- Dow FILMTEC™ Membranes - Form No. 609-00204-1108.

41. Sea Water element SW30HR-370/34i- Dow FILMTEC^{TM} Membranes - Form No. 609-00204-1108.
42. Sea Water element SW30HR-380- Dow FILMTEC^{TM} Membranes - Form No. 609-00204-1108.
43. Zhao, G., Hu, R., Zhao, X., He, Y. & Zhu, H. High flux nanofiltration membranes prepared with a graphene oxide homo-structure. *J. Membr. Sci.* **585**, 29–37 (2019).
44. van Duin, A. C. T., Dasgupta, S., Lorant, F. & Goddard, W. A. ReaxFF: A Reactive Force Field for Hydrocarbons. *J. Phys. Chem. A* **105**, 9396–9409 (2001).
45. Kim, S.-Y. & van Duin, A. C. T. Simulation of Titanium Metal/Titanium Dioxide Etching with Chlorine and Hydrogen Chloride Gases Using the ReaxFF Reactive Force Field. *J. Phys. Chem. A* **117**, 5655–5663 (2013).
46. Ostadhossein, A. *et al.* ReaxFF Reactive Force-Field Study of Molybdenum Disulfide (MoS_2). *J. Phys. Chem. Lett.* **8**, 631–640 (2017).
47. Chenoweth, K., van Duin, A. C. T. & Goddard, W. A. The ReaxFF Monte Carlo Reactive Dynamics Method for Predicting Atomistic Structures of Disordered Ceramics: Application to the Mo3VOx Catalyst. *Angew. Chem. Int. Ed.* **48**, 7630–7634 (2009).
48. Ingebrigtsen, T. & Toxvaerd, S. Contact Angles of Lennard-Jones Liquids and Droplets on Planar Surfaces. *J. Phys. Chem. C* **111**, 8518–8523 (2007).
49. Thomas, J. A. & McGaughey, A. J. H. Water Flow in Carbon Nanotubes: Transition to Subcontinuum Transport. *Phys. Rev. Lett.* **102**, (2009).

50. Sresht, V. *et al.* Quantitative Modeling of MoS_2–Solvent Interfaces: Predicting Contact Angles and Exfoliation Performance using Molecular Dynamics. *J. Phys. Chem. C* **121**, 9022–9031 (2017).
51. Kresse, G. & Furthmüller, J. Efficiency of ab-initio total energy calculations for metals and semiconductors using a plane-wave basis set. *Comput. Mater. Sci.* **6**, 15–50 (1996).
52. Kresse, G. & Furthmüller, J. Efficient iterative schemes for ab initio total-energy calculations using a plane-wave basis set. *Phys. Rev. B* **54**, 11169–11186 (1996).
53. Perdew, J. P., Burke, K. & Ernzerhof, M. Generalized Gradient Approximation Made Simple. *Phys. Rev. Lett.* **77**, 3865–3868 (1996).
54. Grimme, S. Semiempirical GGA-type density functional constructed with a long-range dispersion correction. *J. Comput. Chem.* **27**, 1787–1799 (2006).
55. Berendsen, H. J. C., Postma, J. P. M., van Gunsteren, W. F., DiNola, A. & Haak, J. R. Molecular dynamics with coupling to an external bath. *J. Chem. Phys.* **81**, 3684–3690 (1984).
56. Kwac, K. *et al.* Multilayer Two-Dimensional Water Structure Confined in MoS_2. *J. Phys. Chem. C* **121**, 16021–16028 (2017).
57. Grdadolnik, J., Merzel, F. & Avbelj, F. Origin of hydrophobicity and enhanced water hydrogen bond strength near purely hydrophobic solutes. *Proc. Natl. Acad. Sci.* **114**, 322–327 (2017).